Soil Dynamics and Earthquake Engineering 177 (2024) 108331

Contents lists available at ScienceDirect

Soil Dynamics and Earthquake Engineering

journal homepage: www.elsevier.com/locate/soildyn

# On railway track receptance

Angie C. Lamprea-Pineda [a,*], David P. Connolly [a,**], Alexandre Castanheira-Pinto [b], Pedro Alves-Costa [b], Mohammed F.M. Hussein [c], Peter K. Woodward [a]

[a] Institute for High Speed Rail and System Integration, University of Leeds, Leeds, LS2 9JT, UK
[b] Faculty of Engineering, University of Porto, Porto, 4099-002, Portugal
[c] Department of Civil and Environmental Engineering, Qatar University, Doha, 2713, Qatar

ARTICLE INFO

*Keywords:*
Railway dynamic track stiffness
Railway track receptance
Periodic 3D modelling
Railroad track dynamics
Ground-borne noise and vibration

ABSTRACT

Railway track dynamic stiffness is the relationship between track deflection and loading frequency. Its inverse, also known as receptance, is an important quantity that affects the track's dynamic response under moving trains and noise and vibration characteristics. Despite its importance, there has been limited detailed study into receptance at lower frequencies ($< 1000\,Hz$). Thus, this paper contributes two main novelties. The first is the presentation of a novel numerical approach well-suited to receptance calculation, and secondly, a parametric study identifying the key frequencies associated with different track components. The new approach is first presented, which uses a 3D periodic domain coupled with perfectly matched layers and is solved in the frequency-wavenumber domain. It is well-suited to the problem because it can capture dynamic wave propagation within the complex geometries associated with each track component, while using an efficiently-sized domain. The model is validated in terms of its ability to capture the dynamic response of 3D periodic structures, and also the behaviour of a railway track. It is then used to study the effect of two common modelling assumptions (beam-on-elastic foundation and symmetry) on the calculation of track receptance. It's shown that ignoring wave propagation in the subgrade-earthwork layers induces errors in the $\approx 80-300\%$ range at frequencies below $200\,Hz$, and errors of $\approx 30\%$ in the $200-440\,Hz$ range. It is also shown that the assumption of track centreline symmetry ignores some track bending modes and can also introduce errors ($\approx 20\%$) at frequencies up to $1000\,Hz$. Finally, the effect of the most common ballasted track components on receptance are analysed and new knowledge is presented regarding the typical frequency ranges associated with each.

## 1. Introduction

The dynamic characteristics of a railway track play an important role in its interaction with rolling stock and are closely connected to short term and long term behaviour (settlement) [1,2]. Thus, dynamic stiffness is key parameter reflecting the entire system's quality and performance, which depends on its component's individual and collective behaviour. Track stiffness can be divided into two categories: static and dynamic. In both cases, it is expressed as the ratio between the applied force and the corresponding deformation of the structure [3–5]. However, the force and its resulting deflection are static in the former instance, whereas dynamic and frequency-dependent in the second case. Although both are relevant for track design and maintenance, dynamic stiffness is a key parameter for understanding railway dynamics issues. These include ground-borne noise and vibration at low-frequencies, track dynamics problems at mid-frequencies, and rolling noise issues at high-frequency ranges [6,7].

Dynamic stiffness is commonly studied via its inverse, 'receptance' (also referred to as 'compliance', 'dynamic flexibility' or 'force-displacement transfer function'). Receptance analysis enables the characterisation of railway systems and their components in terms of frequencies influencing the track behaviour. These frequencies are typically referred to as frequencies of resonance and are associated to a 'mode' of the structural vibration. Receptance can be used to identify various structural properties such as stiffness, damping and potentially component dimensions, as well as changes in these parameters and their overall relationship with the global system behaviour. This information has the potential to be used for assessing the mechanical behaviour of

* Corresponding author.
** Corresponding author.
*E-mail addresses:* cnaclp@leeds.ac.uk (A.C. Lamprea-Pineda), D.Connolly@leeds.ac.uk (D.P. Connolly), amgcpinto@fe.up.pt (A. Castanheira-Pinto), pmbcosta@reit.up.pt (P. Alves-Costa), mhussein@qu.edu.qa (M.F.M. Hussein), P.K.Woodward@leeds.ac.uk (P.K. Woodward).

https://doi.org/10.1016/j.soildyn.2023.108331
Received 25 September 2023; Received in revised form 26 October 2023; Accepted 27 October 2023
Available online 25 November 2023

the track structure, define control strategies for several railway issues, and optimise design of new systems.

Receptance studies have proposed analytical, semi-analytical and numerical approaches to assess the track structure and its components. Perhaps the most comprehensive sensitivity studies on railway track components' behaviour have been conducted using analytical methods, such as beam-on-elastic-foundation (BOEF) formulations. These studies have examined the effect of the excitation position, number of layers, element formulations (beam and damping models), material properties, and support effect [8–11]. This range of analysis is possible due to the simplified modelling approach, which characterises the track system components as beams, a series of elastic elements, and lumped masses. These studies have shown that analytical methods require a certain degree of complexity in their simulation, including a minimum of two layers and discrete supports, in order to be able to capture the main vibration modes [9].

Analytical approaches are unable to fully capture 3D wave propagation effects because they are limited in the structural elements they can be formed from. Therefore, they are well suited to cases where the assumption of a rigid foundation is applicable (e.g. directly-fixed railway track in a tunnel) or noise modelling where vibration is confined within the upper track structure. In an attempt to approximate 3D ground wave propagation [12], implemented flexibility matrices in the track sub-structure, defined in the frequency domain, thus enabling subgrade simulation. Different track support models resting on homogeneous and layered-homogenous mediums were compared with simpler analytical models. Results demonstrated the importance of modelling the ground at frequencies below 400 *Hz*, yielding a receptance result that the viscoelastic foundation of the analytical model could not replicate.

Nevertheless, receptance analyses conducted via analytical or semi-analytical strategies rely on several important approximations of the railway system. For instance, railpad complex geometries are usually simplified into viscoelastic point supports – elements described using minimal material parameters (i.e. stiffness and damping only, in absence of geometrical dimensions); track layers are often combined with equivalent parameters used instead; supporting ground is often simulated via springs-in-series assumptions; among other track components' behaviour ignored during simulation that affects the overall dynamic response.

To address this, numerical approaches such as the finite element (FE) and boundary element (BE) methods have also been used to compute receptance. Numerical techniques can be solved in both frequency and time domain [13]. In the former, receptance is computed by enforcing Fourier transformations during the formulation of the algorithms. Approaches in this domain are widely employed in simulations since they provide a straightforward algebraic formulation. In contrast, time-domain methodologies are solved via iterative integration schemes [14,15]. Following the latter methodology [16], conducted an extensive investigation of the dynamic behaviour of the track, assessing the support effect, material properties, and the location of excitation and observation points on different track types, and comparing the results against field tests. This numerical time-domain model was then combined with sensitivity studies on ballasted tracks to derive equations of the resonant frequencies in Ref. [17]. Similarly [18], used a 3D FEM solved in the time domain to compare two different railpad elements: viscoelastic and solid. However, as the frequency range of interest started at 300 *Hz*, the soil behaviour was not included in the simulation. This sensitivity analysis on railpads was extended in Ref. [19], including parameters such as the toe load, temperature effect, aging conditions, and railpad type. Additionally [20], studied the wheel-rail impact problem in the time domain by comparing two wheel-track interaction models, the beam and continuum FE. The former used a discretised Timoshenko beam in the rail and sleeper formulation, whereas the latter employed 3D solid elements. Although both cases simulated railpad and ballast via spring elements, the rail is supported at a single point in the beam model and over an area in the solid model. Overall, findings indicated that solid elements can approximate receptance more accurately than the beam model. The frequency range was broader in this case, ranging from 10 to 3000 *Hz* and the subgrade was not included in the formulation.

Although numerical methods potentially provide more flexibility to model the true geometry of a railway track compared to analytical and semi-analytical methods, they are computationally demanding. In order to reduce the computational effort while still delivering accurate approximations of the structure's behaviour, periodic strategies are a promising solution. These approaches take advantage of the periodic or repetitive characteristics of the system, thus reducing the domain under consideration and, in turn, reducing the computational resources and increasing the computational efficiency. Among the various periodic approaches, the 2.5D Finite Element (FE) has been widely applied for railway track simulations [21–25]. This method requires simplifying the structure into a 2D slice. Assuming this slice repeats along the longitudinal or train passage direction, a fully 3D response is recovered via Fourier transformations. For example, combining this approach with the boundary element method (BE) [26], studied the effects on ballasted tracks with mats via receptance analysis. However, since the study focused on lower-track components, only low-frequency ranges ($f < 150$ *Hz*) were considered. Despite providing computational benefits, the 2.5D only meshes the cross-section of the structure and assumes a homogeneous behaviour in its longitudinal direction. Thus, the method fails to capture discrete rail support effects.

As an alternative periodic approach to 2.5D, the 3D FE wave propagation technique enables the simulation of discrete support behaviour [27–29]. This is achieved by discretising the structure into a 3D slice, and enforcing Floquet transformations solved via Eigenvalue problems in the wavenumber-frequency domain, i.e. modal analysis. Using this method [30], conducted low-frequency range ($f < 100$ *Hz*) receptance analysis to study several substructure track properties, such as transition zone problems and the effect of different mats. Although this method offers a flexible geometry, it relies on extracting Eigenmodes and demanding additional strategies to optimise the solution process.

To address these challenges, this paper provides two main novelties: (1) the presentation of a new numerical approach tailored to receptance calculation on ballasted tracks, and (2) a comprehensive study identifying the key frequencies associated with different track components. First the paper introduces the theory of receptance, resonant frequencies and vibration modes. Then, the numerical approach and its validation are presented. This employs a computationally efficient periodic technique that simulates the structure as a 3D FE-PML slice (finite elements coupled to perfectly matching layers to simulate both the track and the ground, respectively) and later recovers the complete structure's response via a direct inversion and the application of Floquet's theorem. Next, a sensitivity analysis of the various track components is conducted, including the effect of the rail section, railpad stiffness, sleeper material, under sleeper pad (USP) application, ballast stiffness, embankment simulation, and subgrade stiffness. Finally, the track components' effect on receptance is assessed, allowing for the definition of typical frequency ranges associated with each. Using the proposed 3D FE-PML periodic technique, it provides in-depth insight into the effects of track components on receptance, which complements the research conducted in Refs. [9,12,16].

## 2. Receptance concepts

Receptance is a frequency response function (FRF) which allows for an understanding of the dynamic track behaviour in terms of deflection. The various vibration modes of the track are related to specific resonant frequencies and strongly depend upon their various components' properties [10,16,31]. The conventional definition of receptance is described in **Eq. (1)**:

$$\alpha^2(\omega) = \frac{S_{ww}(\omega)}{S_{FF}(\omega)} \tag{1}$$

where $\alpha$ is receptance or displacement amplitude resulting from the unit impulse excited with frequency $\omega$; and $S_{ww}$ and $S_{FF}$ are the auto-spectrum of the displacement and the force, respectively [16]. In addition to receptance function, which expresses the response as displacements, two additional FRFs sometimes computed during in-situ testing are: mobility and accelerance, in terms of velocities and accelerations, respectively. See Table 1 where all frequency functions are mutually related by the angular frequency $\omega$. Note that although FRFs are inherently complex functions, the focus of this paper is on the absolute response of the track. Thus, **Eq.** (1) and Table 1 depict auto-spectrum and absolute results, respectively (i.e. FRF complexity vanishes). Alternatively, if considering FRFs' complexity, derivations in Table 1 should incorporate the imaginary component in terms of $i\omega$. Similarly, to describe the complexity in **Eq.** (1), the cross-spectrum between the displacement and the force $S_{wF}$ can be included, resulting in $\alpha(\omega) = S_{wF}(\omega)/S_{FF}(\omega)$ – see Ref. [31].

### 2.1. Vibration frequencies and modes

The properties and position of the track components define the complete structural vibration. Based on this, three frequency ranges can be identified according to their main effect on the structural components [5]:

- Low frequencies, $f = [0 - 300]\,Hz$, mostly influencing the track substructure.
- Mid frequencies, $f = [300 - 800]\,Hz$, affecting all superstructure components except the rail.
- High frequencies, $f > 800\,Hz$, which mainly impact the rail behaviour.

The important track frequencies can be discretised into those below. The corresponding mode shapes are shown in **Fig.** 1 using simplified beam-on-elastic foundation visual representation to assist understanding. From low to high frequency:

(a) Subgrade resonance $f_{\text{subgrade}}$. Although mainly governing the low-frequency range, the subgrade properties also influence the response up to the mid-range [12]. At this frequency, the ballasted track has its maximum deformed shape, with all layers adopting a similar deformed shape to the subgrade, leading to a wide bending shape, as shown in **Fig.** 1(a).

(b) Full track resonance $f_{\text{full-track}}$. Often found at low- and lower mid-ranges, at this frequency, the rail and the sleeper mass move vertically in phase on the flexibility of the lower track layers (i.e. ballast and sub-ballast). The amplitude of receptance is well-damped at $f_{\text{full-track}}$, mainly due to the ballast, which makes its receptance peak flat [32]. The vibration mode generated at this frequency is similar to that displayed at $f_{\text{subgrade}}$, however its deflection is lower with reduced subgrade deflection – see Fig. 1 (b). Despite its characteristic deformed shape, due to the wave propagation effect of the subgrade, $f_{\text{full-track}}$ can be challenging to identify.

(c) Rail frequency $f_{\text{rail}}$. This receptance frequency occurs at frequencies above $f_{\text{full-track}}$, between the mid- and high-frequency ranges. At this frequency, the rail and the sleeper mass move in opposite directions (i.e. in antiphase) on the flexibility of the railpad [8,9] – as illustrated in Fig. 1(c). Often, several peaks with similar mode shapes to $f_{\text{rail}}$ can be found at different frequencies, resulting in multiple $f_{\text{rail},i}$. Lower frequency peaks $f_{\text{rail},1}$ are mostly related to the ballast properties. On the contrary, peaks located at higher ranges are related to a stiff railpad behaviour and the rail frequency can instead be defined as the railpad frequency, i.e.

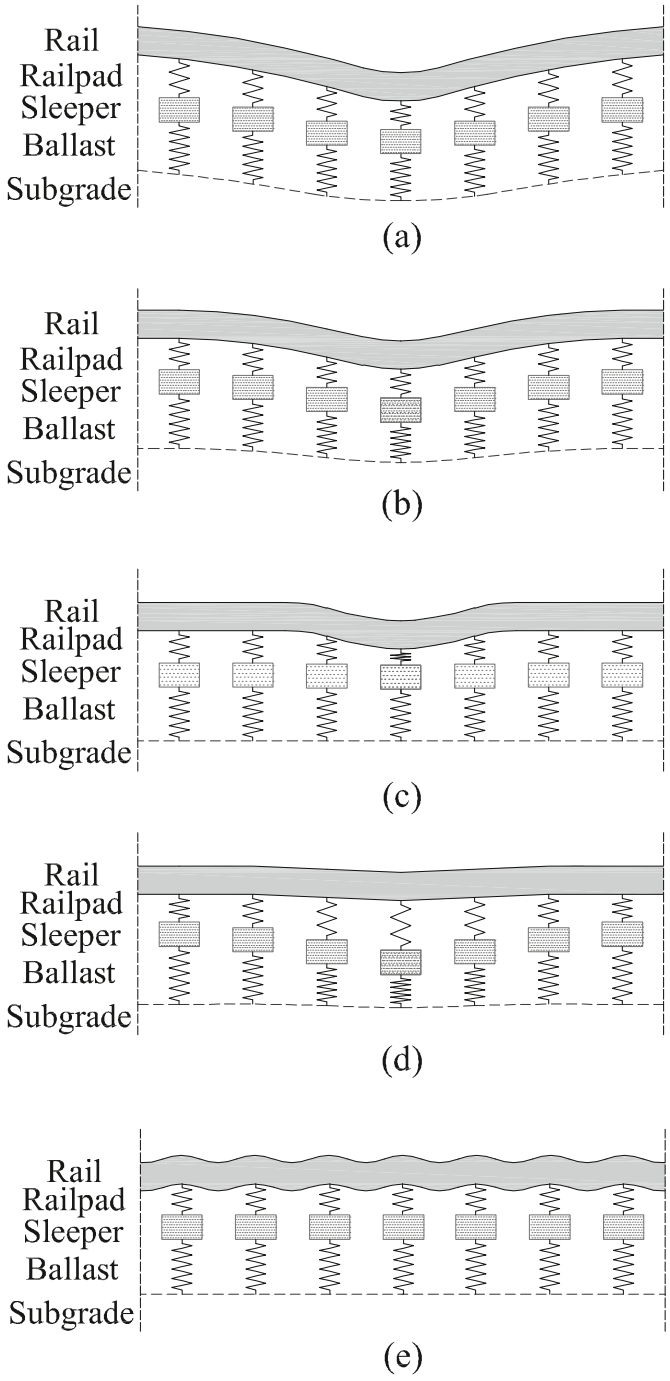


**Fig. 1.** Generalised mode shapes of a track on a flexible foundation. Corresponding to: (a) subgrade resonance, (b) full-track resonance, (c) rail resonance, (d) sleeper anti-resonance, and (e) pin-pin resonant frequency.

**Table 1**
Frequency response definition and relationships [16].

| | Receptance (or Compliance) | Mobility (or Admittance) | Accelerance (or Inertance) |
|---|---|---|---|
| Response definition | Displacement/Force | Velocity/Force | Acceleration/Force |
| Equation | $\alpha = \frac{Y}{\omega} = \frac{\chi}{\omega^2}$ | $Y = \omega\alpha = \frac{\chi}{\omega}$ | $\chi = \omega^2\alpha = \omega Y$ |
| Unit | [m/N] | [m/Ns] | [m/Ns$^2$] |
| Inverse | Dynamic stiffness | Mechanical impedance | Apparent mass |

$f_{\text{rail},2} = f_{\text{railpad}}$. Note that for soft railpads, $f_{\text{railpad}}$ value is low, likely combining into a single peak with $f_{\text{rail},1}$.

(d) Sleeper anti-resonance $f_{\text{sleeper}}$ is a low magnitude region separating both consecutive resonant frequencies $f_{\text{full-track}}$ and $f_{\text{rail}}$. At this frequency, the amplitude of displacement drops, reaching a pronounced minimum. Due to this behaviour, which is analogous to the pronounced maxima found in $f_{\text{full-track}}$ and $f_{\text{rail}}$, this frequency is known as an anti-resonance. At this frequency, the rail displays minimal movement, while the sleeper moves vertically in parallel to the railpad and the ballast [8,12] – as described in Fig. 1(d).

(e) Pin-pin resonant frequency $f_{\text{pin-pin}}$. Similar to $f_{\text{rail}}$, at $f_{\text{pin-pin}}$ the rail is in antiphase with its discrete supports. However, at the pin-pin resonance, the bending shape of the rail is defined by the support spacing [8,12]. Due to the low damping provided by the rail, the receptance peak lies in a narrow frequency range [32]. Fig. 1(e) shows the first order pin-pin frequency $f_{\text{pin-pin}}$.

To illustrate the reading and interpretation of receptance curves, Fig. 2 highlights the main resonant frequencies of a ballasted track resting on a homogeneous half-pace. Receptance curves, computed at mid-span and on support of the rail, are displayed in different formats: (a) linear-linear, (b) linear-log (semi-log), and (c) log-log scale. Also, the effect of the railpad stiffness is shown at mid-span and above sleeper receptance curves: soft railpads result in a single $f_{\text{rail}}$, while stiff railpads leads to multiple $f_{\text{rail},i}$. In addition, it is seen that the railpad does not significantly affect the $f_{\text{pin-pin}}$ value at mid-span of the rail, however, stiff railpads increase the amplitude of the response at this frequency. On the contrary, above the sleeper, $f_{\text{pin-pin}}$ and its amplitude are lower for the soft compared to stiff railpads. In the linear-linear case, results are scaled equally on both axes, meaning readability can be challenging if the stiffness changes significantly throughout the track-ground structure. For instance, when a stiff track rests on a much softer ground, the amplitude of the response at lower frequencies is larger than that at higher frequencies. Therefore a linear-linear scale is usually most suitable for studying lower frequency energy.

Alternatively, logarithmic formats can help improve the readability of receptance curves which oscillate over the wider amplitude (and frequency) ranges. In the linear-log scale, the horizontal axis (frequency) is linear, while the vertical (receptance amplitude) is in logarithmic format. This helps highlight changes in amplitude in the mid frequency range. Finally, a log-log format is useful for studying changes in the high frequency range because it amplifies oscillations at high frequency, which are small compared to the low frequency energy. Therefore it is commonly used for noise analysis. Considering the focus of this paper is on the effect of track components on receptance, the linear-linear scale is predominantly used hereafter.

### 2.2. Receptance testing configuration

Experimentally, receptance can be computed via an instrumented hammer test, which excites the track – either the rail or the sleeper. This results in time-history amplitudes recorded through accelerometers (or geophones) that, along with the time-domain excitation signal, are later

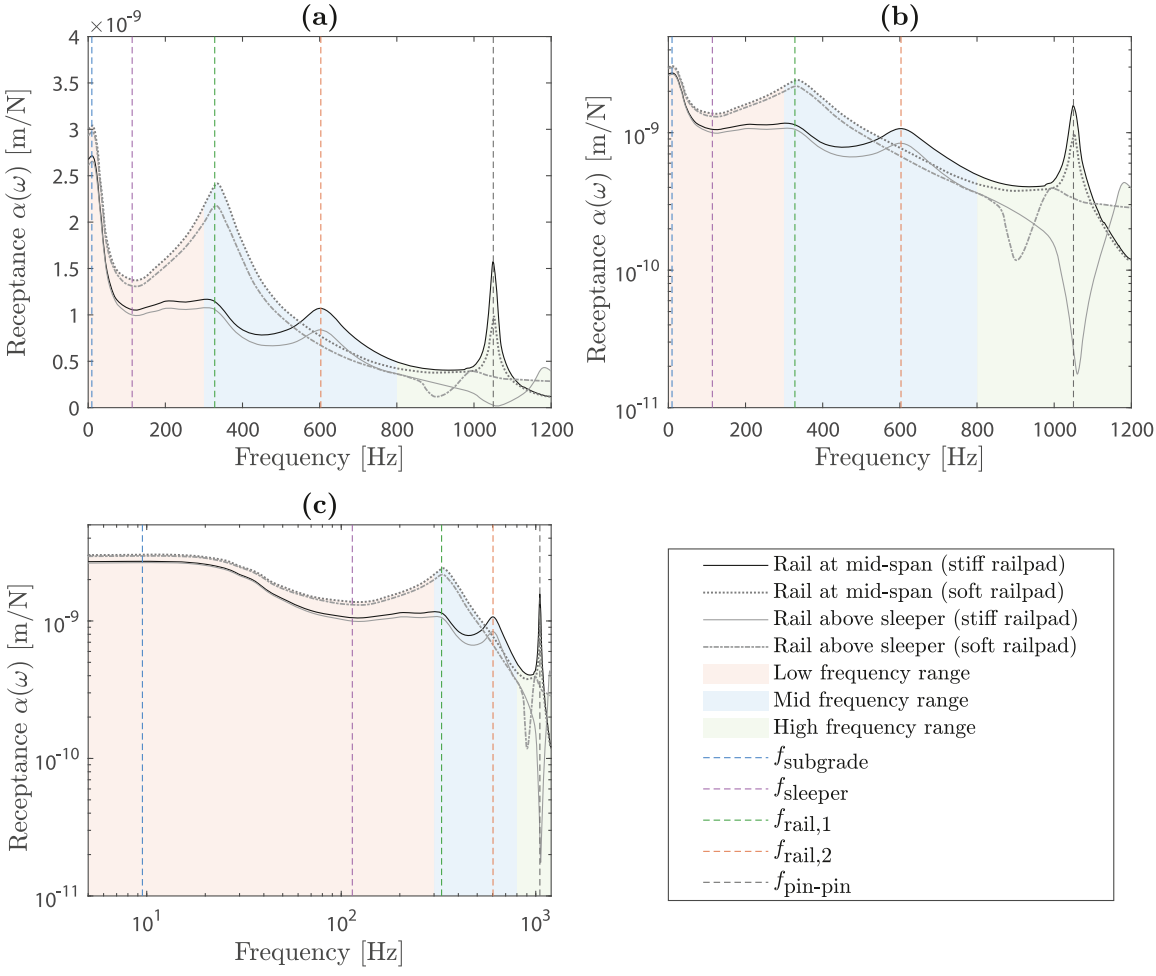


**Fig. 2.** Ballasted track receptance curves with resonant frequencies highlighted: (a) linear scale, (b) semi-log scale, and (c) log-log scale.

processed to obtain the frequency-domain response and compute the receptance function [16,21,33,34]. However, when performing in-situ receptance testing, it is challenging to measure the response at the exact track position where the hammer excitation is applied. Thus, in contrast to the idealised receptance procedure performed in numerical models, in-situ transfer functions (also known as cross-receptance) require the sensor position to differ from the excitation. This results in lower deflection amplitudes in the latter case compared to the former.

Fig. 3 shows some typical in-situ receptance test configurations, highlighting the excitation and sensor locations, including: rail above the sleeper (blue), rail at mid-span or between two sleepers (red), sleeper shoulder (yellow), and sleeper centre (green). The choice of excitation position plays a significant role in the receptance curve characteristics, particularly at high-frequency ranges. For example, when the excitation is applied at mid-span of the rail, the response at $f_{\text{pin-pin}}$ is high, resulting in an upper peak describing a large deflection and a resonant frequency. In contrast, when the force is on the rail above the support or directly on the sleeper, the pin-pin occurs at a lower peak, resulting in a stiff track and an anti-resonance [8,32,35] – see Fig. 2.

## 3. Numerical modelling

### 3.1. Motivation

Beam-on-elastic-foundation (BOEF) approaches are widely employed when studying railway track dynamics. Most commonly they assume the track response can be approximated using a single-layer continuous beam supported by springs-in-series (representing the rails and the underlying track layers, respectively), thus, offering a straightforward and computationally efficient approach. Although the underlying formulation can be extended to incorporate discrete sleeper effect and additional track components in the form of lumped masses and elastic layers, it is difficult to accurately capture 3D wave propagation within the track, which is crucial for simulating receptance – see Fig. 4.

To overcome this, the track requires 3D simulation, faithfully capturing the geometry of each track component. The challenges associated with using BOEF for receptance, and how they are overcome using 3D modelling are:

- Rail support conditions. Although able to represent their discrete support effect, BOEF often defines railpad components via springs and dampers [36,37]. These elements are described by minimal parameters (stiffness and damping only), ignoring the actual dimensions of the components and assuming small and rigid point supports spaced by length $d$ – see Fig. 4(a). Instead, FEM employs elements defined by several material (stiffness, damping, Poisson's, density, etc.) and geometrical parameters (length, height, width), thus providing a more realistic representation of the railway system's behaviour [38] – as shown in Fig. 4(b). In this, a ballasted track is simulated via solid finite elements, which allows for actual railpad dimensions with effective support spacing (from end to end) $d$ differing from the support spacing (from mid-to mid-point) $d^*$.
- Track components. BOEF can consider various track components via multi-layer models. However, it typically combines several layers (e.g. ballast and sub-ballast) into equivalent parameters and disregards some of their mechanical behaviour and real dimensions – Fig. 4(a) shows lower track components combined into the single layer 'foundation'. In contrast, FEM complexity facilitates several track components' mechanical behaviour representation [14,39] – as illustrated in Fig. 4(b), in where ballast and sub-ballast layers are simulated separately.
- Subgrade conditions. BOEF employs springs in series elements to simulate the soil behaviour, thus, it is unable to reproduce the wave propagation within the soil and leads to an inaccurate dynamic track-ground response – see Fig. 4(a). Alternatively, FEM allows for a more accurate mechanical representation of the supporting soil, considering their actual material properties, a closer geometrical domain, and its wave propagation effect [15,40] – see Fig. 4(c).

### 3.2. Model overview

Although 3D simulation is advantageous for receptance computation compared to BOEF, small element sizes are required to capture waves propagating in the higher frequency range, while at the same time, large domains are required to capture waves propagating at the lower frequency range. Also, the dynamic nature of the problem means boundary reflections must be minimal across the frequency range. A model is thus developed capable of meeting these conditions. It uses a periodic approach to reduce the effective domain length required for simulation in the direction of train passage, while also eliminating the need for an absorbing boundary in this plane. Then, to minimise boundary reflections in the remaining two directions, a high-performance perfectly matched layer solution is implemented in the frequency-wavenumber domain.

This paper employs the direct periodic method, DPM, proposed by Ref. [41], a technique that exploits the repetitive or invariant nature of railway structures to study large domains (e.g. infinitely extending tracks). In railway systems, periodicity is found by considering both material and geometrical properties repeat themselves at a regular interval, known as the periodic length $d$. For instance, in ballasted tracks, periodicity is defined by the repeated pattern of the sleepers [42,43] – see Fig. 5(a). In contrast, in slab tracks, the periodicity is found in the discrete rail-seats [44,45] or the slab units arrangement [46–49], as

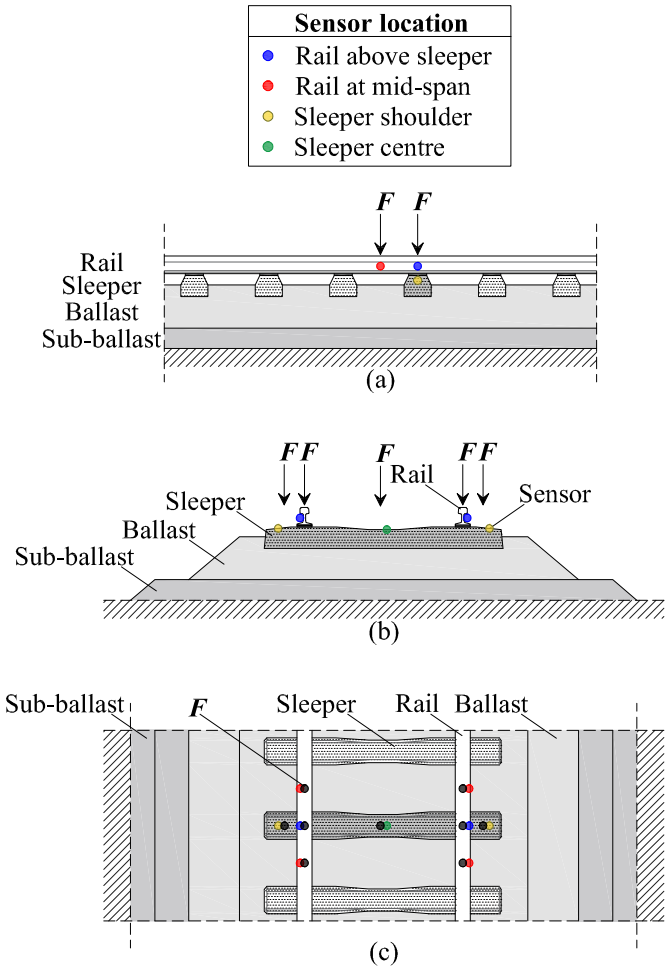


**Fig. 3.** Typical receptance excitation and accelerometers positions, (a) longitudinal view, (b) transversal view, and (c) birdseye view.

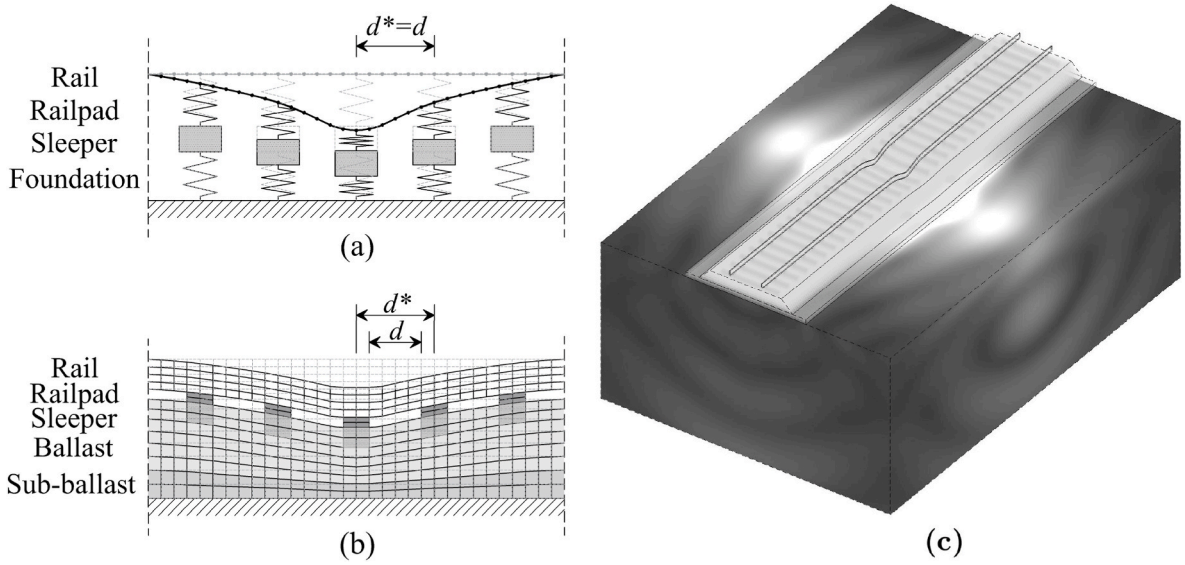


**Fig. 4.** Track simulation comparison: (a) track on rigid support – BOEF model, (b) track on rigid support – FE model, and (c) track on flexible support – wave propagation effect (mesh omitted for visibility).

shown in Fig. 5(b) and (c), respectively.

Since the properties repeat themselves every length $d$, only a portion $\widetilde{\Omega}$ of the total structure $\Omega$ is required in the simulation. Then, the total response of the latter is retrieved by enforcing compatibility conditions at the boundaries of the former. This restricted domain is often known as the generic or unit cell, and it is assumed to be infinitely repeated, forming the entire structure or total domain [11]. Due to the simplification in the study domain, the periodic approach allows for computing accurate results with minimal computational effort and shorter simulation times compared to fully 3D modelling techniques. Procedure for calculating the total track response via the direct periodic method comprises three steps – Fig. 6:

(a) Computation of the reference cell response in the wavenumber-frequency domain – see Fig. 6(a). Firstly, the system of equations of motion of the restricted domain is defined in the wavenumber and frequency domain. Then, periodic boundary conditions at the restricted domain's back and front face are enforced, modifying the equilibrium equations and allowing for its response computation.
(b) Response of all cells in the wavenumber-frequency domain – see Fig. 6(b). Once the reference cell response is obtained, periodic conditions are again imposed, and the response of the remaining cells in the wavenumber-frequency domain is computed.
(c) Total structure response in the space-frequency domain – see Fig. 6(c). Fourier transformation is used to transform the total structure response in the wavenumber domain back to space.

### 3.3. Solution process

The DPM method allows for the computation of the entire periodic structure $\Omega$ by simply studying the behaviour of a discretised domain $\widetilde{\Omega}$, i.e. the reference cell response $\widetilde{u}_{n=0}$. Next, via enforcement of a periodic condition – defined by Floquet theory [45,50–52], the total domain response at all cells $\widetilde{u}_n$ is obtained, as shown in **Eq.** (2):

$$\widetilde{u}_n\left(x,y,z,k_1,\omega\right)=\widetilde{u}_{n=0}(\widetilde{x},\widetilde{y},\widetilde{z},k_1,\omega)e^{ik_1nd} \tag{2}$$

where $s=\{x,y,z\}$ and $\widetilde{s}=\{\widetilde{x},\widetilde{y},\widetilde{z}\}$ are the space vectors defining $\Omega$ and $\widetilde{\Omega}$, respectively. Similarly, $\widetilde{u}_n$ and $\widetilde{u}_{n=0}$ are the displacements of the total $\Omega$ and discretised $\widetilde{\Omega}$ domain, respectively. The tilde notation ' $\sim$ ' in $\widetilde{u}_n$, is employed to represent the wavenumber-frequency domain $(k_1,\omega)$, and the number of the cell is defined by $n$, being $n=0$ the reference cell, and $n\neq 0$ the remaining structure; and $d$ is the thickness of the reference cell in the periodic direction – $x$ axis or longitudinal direction. Since periodicity is assumed only in the longitudinal direction, the wavenumber response is presented solely around this direction and $\widetilde{x}\neq x$. Similarly, the vectors corresponding to the transversal and vertical coordinates remain constant, i.e. $y=\widetilde{y}$ and $z=\widetilde{z}$, and their corresponding wavenumber response, $k_2$ and $k_3$, are not considered in **Eq.** (2).

In order to properly enforce the periodic condition described in **Eq.** (2), the displacements at the front face of the reference cell must be formulated according to those at the back and the periodic condition $e^{ik_1d}$, see **Eq.** (3):

$$\begin{aligned}&\widetilde{u}^{front}_{n=0}(\widetilde{x}=d,y=\widetilde{y},z=\widetilde{z},k_1,\omega)\\&=\widetilde{u}^{back}_{n=0}(\widetilde{x}=0,y=\widetilde{y},z=\widetilde{z},k_1,\omega)e^{ik_1d}\end{aligned} \tag{3}$$

where $\widetilde{u}^{front}_{n=0}$ and $\widetilde{u}^{back}_{n=0}$ refer to the front and back border displacements of the reference cell, respectively.

Enforcement of the periodic conditions described in **Eqs.** (2)-(3), ensures the continuity of the displacements at the boundaries of each cell, allowing for the displacements of the back and front faces of the $n^{th}$ cell to be continuous at the front of the $n^{th}-1$ cell and back of the $n^{th}+1$ cell, respectively – see **Fig.** 6(b) and **Eq.** (4):

$$\begin{aligned}\widetilde{u}^{back}_{n}&=\widetilde{u}^{front}_{n-1}\\\widetilde{u}^{front}_{n}&=\widetilde{u}^{back}_{n+1}\end{aligned} \tag{4}$$

Once obtained the $k_1$ domain response for all $n$ cells, $\widetilde{u}_{cell,n}$ (**Eq.** (2)), it can be transformed back to space domain $x$ through the Fourier transform in **Eq.** (5):

$$\widehat{u}(x,y,z,\omega)=\frac{1}{2\pi}\int_{-\infty}^{\infty}\widetilde{u}_n(x,y,z,k_1,\omega)e^{ik_1x}\mathrm{d}k_1 \tag{5}$$

where $\widehat{u}$ is the displacement of the total domain in the space-frequency domain $(x,\omega)$, as described by the hat notation ' $\widehat{}$ '.

#### 3.3.1. Reference cell definition and response

Firstly, the reference cell response $\widetilde{u}_{n=0}$ must be computed in order to retrieve the total structural response $\widehat{u}$. To do so, the system of equations

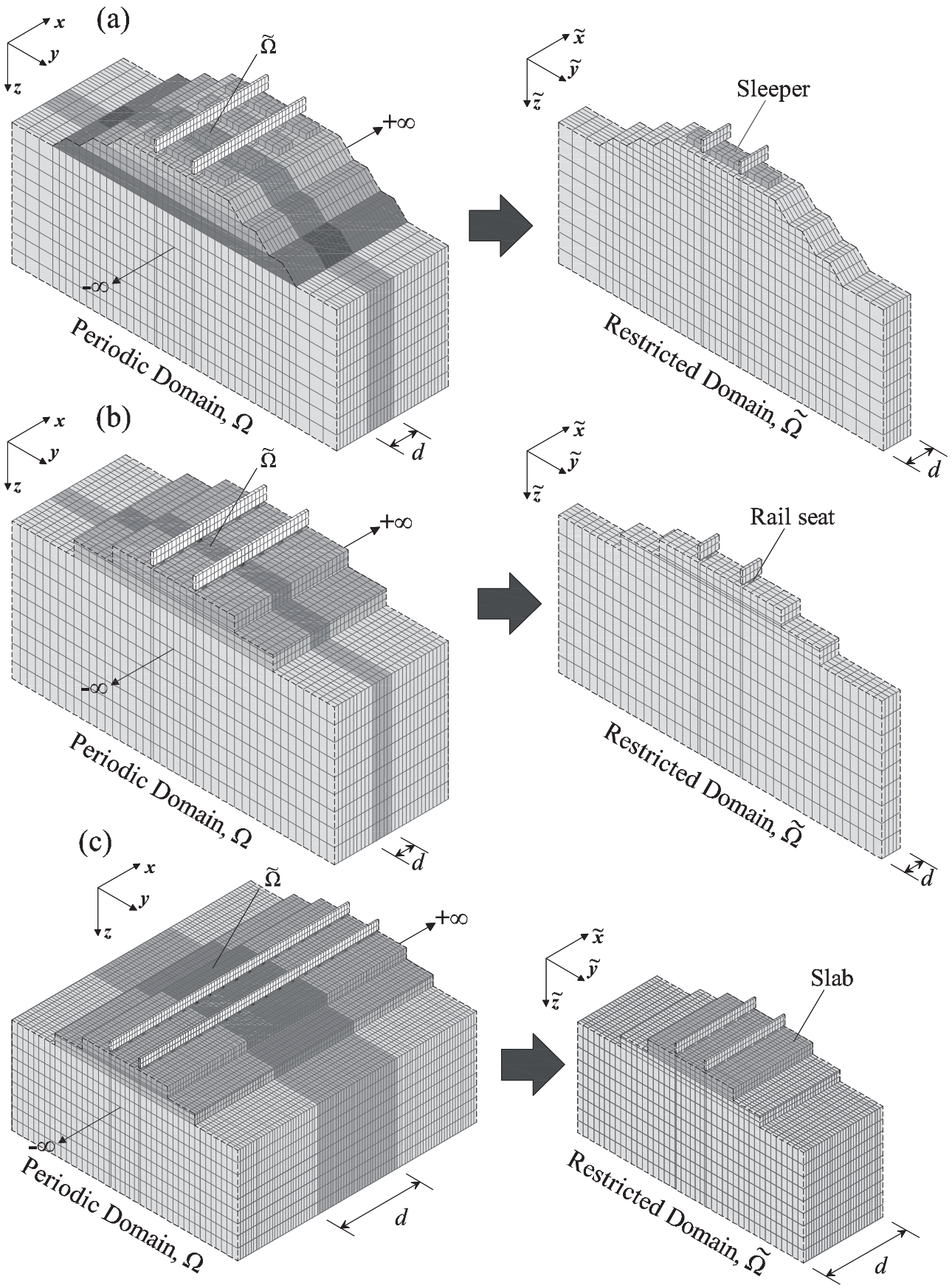


**Fig. 5.** Overview of 3D periodic and generic domains, (a) ballasted track – periodicity due to sleeper placement, (b) slab track – periodicity due to rail-seats, (c) slab track – periodicity due to the discontinuous slabs [11].

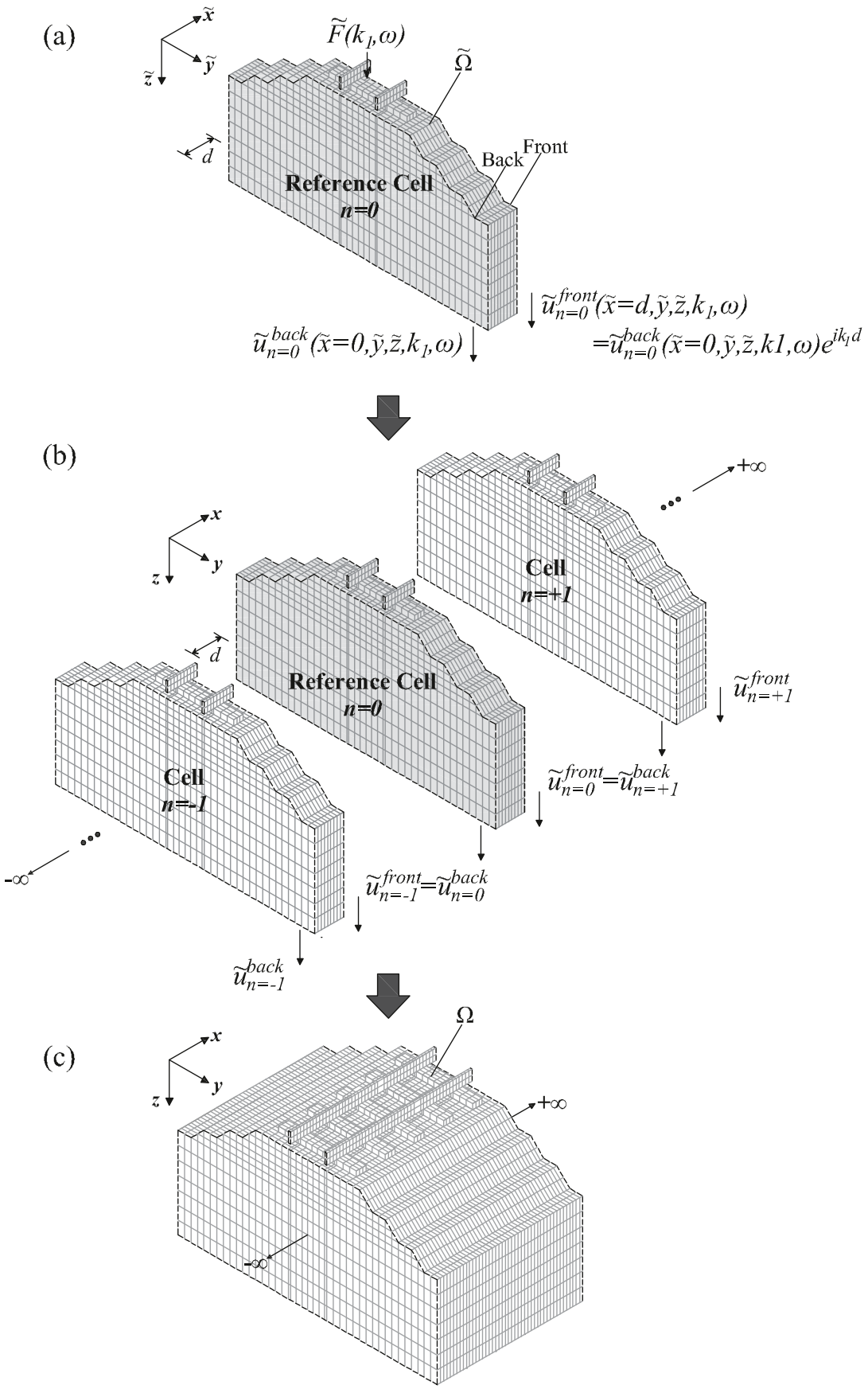


**Fig. 6.** Direct periodic method overview: (a) reference cell response in wavenumber-frequency domain, (b) all cells' response in wavenumber-frequency domain, and (c) total response in space-frequency domain.

of motion of the restricted domain must be formulated and solved in the wavenumber-frequency domain. **Eq.** (6) shows the set of equilibrium equations of the reference cell $n = 0$, in matrix format:

$$[\widetilde{D}_{n=0}]\{\widetilde{u}_{n=0}\} = \{\widetilde{F}_{n=0}\} \tag{6}$$

where $\left\{\widetilde{F}_{n=0}\right\}$ and $\left\{\widetilde{u}_{n=0}\right\}$ are the vectors of the moving external force and displacements of the reference cell, respectively. The dynamic stiffness matrix (DSM) of the reference cell $\left[\widetilde{D}_{n=0}\right]$ is computed by combining its stiffness $k$, damping $c$ and mass $m$ parameters, in the frequency domain $\omega$, as shown in **Eq.** (7):

$$[\widetilde{D}_{n=0}] = [K_{n=0}] - \omega^2[M_{n=0}] \tag{7}$$

in where $[K_{n=0}]$ and $[M_{n=0}]$ are the complex stiffness and mass matrices of the cell $n = 0$. The damping formulation is accounted within $[K_{n=0}]$ via the hysteretic model [11] in **Eq.** (8):

$$[K_{n=0}] = [K](1 + i\eta) \tag{8}$$

where $[K]$ is the real stiffness matrix and $\eta$ is the loss factor of the material and. The stiffness and mass matrices are computed via finite element approaches with **Eqs.** (9) and (10):

$$[K_{n=0}(\tilde{x},\tilde{y},\tilde{z})] = \int_{\tilde{x}}\int_{\tilde{y}}\int_{\tilde{z}} [B]^T[D][B]\mathrm{d}\tilde{x}\mathrm{d}\tilde{y}\mathrm{d}\tilde{z} \tag{9}$$

$$[M_{n=0}(\tilde{x},\tilde{y},\tilde{z})] = \int_{\tilde{x}}\int_{\tilde{y}}\int_{\tilde{z}} [N]^T\rho[N]\mathrm{d}\tilde{x}\mathrm{d}\tilde{y}\mathrm{d}\tilde{z} \tag{10}$$

where $[D]$ is the elasticity or material matrix, $[B(\tilde{x},\tilde{y},\tilde{z})] = [L(\tilde{x},\tilde{y},\tilde{z})][N(\tilde{x},\tilde{y},\tilde{z})]$ is the strain–displacement transformation matrix or matrix of partial derivatives $[L]$ of the shape functions $[N]$, and $\rho$ is the material density. Regarding the force vector $\left\{\widetilde{F}_{n=0}\right\}$, a point load is defined by considering a combination of multiple plane waves [23]. Fig. 7(a) shows the plane wave combination, and their shapes, related to each value of the wavenumber sampling (only the limits and the $j^{th}$ component of $k_1$ are shown). In contrast, Fig. 7(b) presents the resulting point load in the wavenumber domain $\widetilde{F}(k_1)$ obtained after combining the plane waves associated to all wavenumber values. The schematic representation of the point load can be defined via **Eq.** (11):

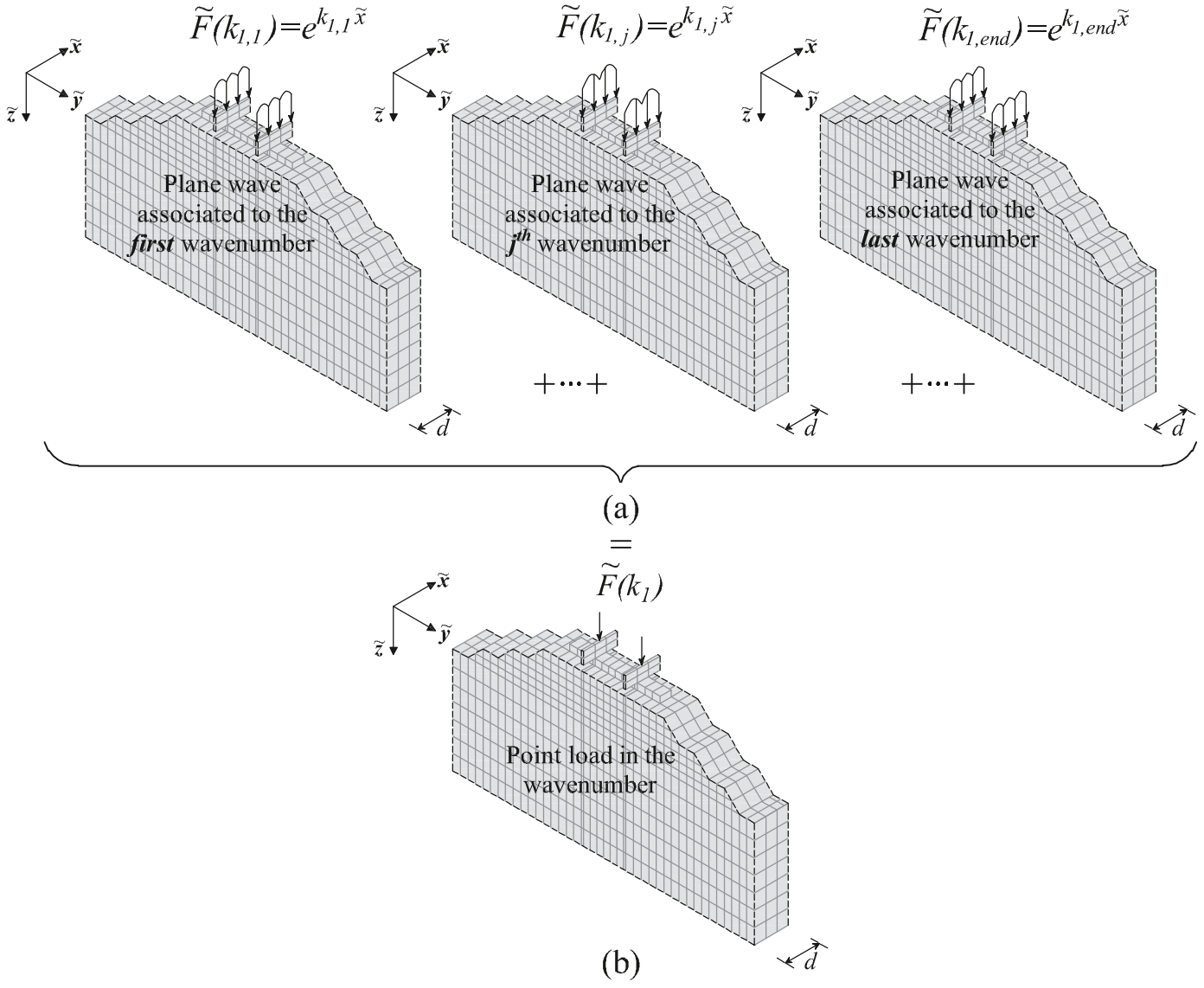


**Fig. 7.** Reference cell subject to a point load decomposed into plane waves: (a) plane wave shapes, and (b) point load in $k_1$ domain.

$$\widetilde{F}(k_1) = Pe^{ik_1\tilde{x}} \tag{11}$$

where $P$ is the magnitude of the force, the exponential term $e^{ik_1\tilde{x}}$ defines the plane waves, and $\tilde{x}$ is the space coordinate, in the longitudinal direction, of the nodes where the plane waves are distributedly applied in the reference cell. Note that **Eq. (11)** is similar to the format used when accounting for multiple axles, derived from the Fourier transform of the force in the space domain depicted in **Eq. (12)**:

$$F(x) = P\delta(x - x_o)e^{i\varpi t} \tag{12}$$

where $\delta(\bullet)$ is a Dirac delta function defining an impulse, $x_o$ is the observation point, $\varpi$ is the oscillating frequency of the excitation. Fourier transformation of the force (from space to wavenumber), results in the removal of the exponential term $e^{i\varpi t}$:

$$\widetilde{F}(k_1) = \int_{-\infty}^{\infty} F(x)e^{-ik_1x}\mathrm{d}x = \int_{-\infty}^{\infty} P\delta(x - x_o)e^{i\varpi t}e^{-ik_1x}\mathrm{d}x = Pe^{-ik_1x_o} \tag{13}$$

Overall, it is important to consider that the plane waves are distributed forces – as shown in Fig. 7. Thus, its equivalent nodal forces are required to define the force vector in the Finite Element problem.

### 3.3.2. Boundary conditions and response

Before solving the system in **Eq. (6)**, periodic boundary conditions at the restricted domain's back and front face are enforced, rearranging the equilibrium equations and allowing for its response computation. This rearrangement can be seen as a compatibilisation procedure, since periodic conditions are enforced at the back ($\tilde{x}$= 0) and front ($\tilde{x}$= $d$) faces of the reference cell – see Fig. 6. **Eq. (14)** recalls the periodic condition to be imposed within $n$ = 0:

$$\{\widetilde{u}_{n=0}^{front}\} = \{\widetilde{u}_{n=0}^{back}\}e^{ik_1d} \tag{14}$$

To allow for continuity in the complete domain, it is necessary to avoid double counting the front contribution of each cell in the total response. This is achieved by taking the contribution of the front nodes of the reference cell to the corresponding back nodes in the dynamic stiffness matrix and the vectors of displacements and forces. **Eq. (15)** and (16) show the compatible system and its inversion to obtain the response of the reference cell in terms of displacements, respectively.

$$\left[\widetilde{D}_{n=0}^{*}(k_1,\omega)\right]\left\{\widetilde{u}_{n=0}^{*}(k_1,\omega)\right\} = \left\{\widetilde{F}_{n=0}^{*}(k_1)\right\} \tag{15}$$

$$\left\{\widetilde{u}_{n=0}^{*}(k_1,\omega)\right\} = \left[\widetilde{D}_{n=0}^{*}(k_1,\omega)\right]^{-1}\left\{\widetilde{F}_{n=0}^{*}(k_1)\right\} \tag{16}$$

where '*' indicates the compatibilisation condition imposed in the vectors and the matrix (dropped in the following computations for visibility).

### 3.3.3. Total structural response

Assuming a periodic behaviour, the track can be thought as a combination of multiple reference cells connected to each other at their ends via enforcement of periodic conditions – see Fig. 6(b). **Eq. (17)** shows the track response $\widetilde{u}$ in the wavenumber-frequency domain:

$$\begin{aligned}&\widetilde{u}(x,y,z,k_1,\omega)\\ &= \widetilde{u}_n(x = \tilde{x} + nd, y = \tilde{y}, z = \tilde{z}, k_1, \omega)\\ &= \widetilde{u}_{n=0}(\tilde{x},\tilde{y},\tilde{z},k_1,\omega)e^{ik_1nd}\end{aligned} \tag{17}$$

where $\widetilde{u}_n$ is the displacement of all nodes of the $n^{th}$ cell, which is computed from the combination of the reference cell displacement $\widetilde{u}_{n=0}$ and the exponential term $e^{ik_1nd}$ defining the periodic condition.

The space vectors describing the reference cell in the longitudinal, transversal and vertical directions are $\{\tilde{s}\} = \{\tilde{x}, \tilde{y}, \tilde{z}\}$, respectively. Alternatively, the space vectors defining the total track response are $\{s\} = \{x,y,z\}$. Note that although the response is computed in the $(k_1,\omega)$ domain, $\{\tilde{s}\}$ and $\{s\}$ are used in the definition of the reference cell and the track response in terms of the $n^{th}$ cell – as shown in **Eq. (17)**. Also, since periodicity is assumed only in the longitudinal direction, the wavenumber response is presented solely around the $x$ direction, and the space vector related to this coordinate depends upon the number of cell $n$ and its length $d$, i.e. $k_1 = k_x$ and $x = \tilde{x} + nd$, respectively. Thus, the vectors corresponding to the transversal and vertical coordinates remain unchanged, i.e. $y = \tilde{y}$ and $z = \tilde{z}$, and no wavenumber samplings are required along these directions.

Once the response in the $(k_1,\omega)$ is obtained at all cells, the inverse Fourier transform (**Eq. (18)**) is employed to convert the wavenumber result $\widetilde{f}(k_1)$ back to space domain $f(x)$, as described in **Eq. (19)**:

$$f(x) = \frac{1}{2\pi}\int_{-\infty}^{\infty}\widetilde{f}(k_1)e^{ik_1x}\mathrm{d}k_1 \tag{18}$$

$$\begin{aligned}\widehat{u}(x,y,z,\omega) &= \frac{1}{2\pi}\int_{-\infty}^{\infty}\widetilde{u}_n(x = \tilde{x} + nd, y, z, k_1, \omega)\mathrm{d}k_1\\ &= \frac{1}{2\pi}\int_{-\infty}^{\infty}\widetilde{u}_{n=0}(\tilde{x},\tilde{y},\tilde{z},k_1,\omega)e^{ik_1nd}\mathrm{d}k_1\end{aligned} \tag{19}$$

where $\widehat{u}$ is the total domain response in the space domain. By expanding **Eq. (19)**, it can be seen that the exponential value $e^{ik_1nd}$ is analogous to the exponential $e^{ik_1x}$ in the inverse Fourier transformation shown in **Eq. (18)**.

## 3.4. Soil domain

Vibrations induced by the train passage have two excitation components: quasi-static and dynamic. Although the former, resulting from the vehicle weight, plays an important role at lower frequencies in the near-field, the dynamic excitation caused by train-track interaction dominates the ground vibration levels [11,23,53,54]. To study the wave propagation within the ground, half-space foundation models are useful. However, these models are complex and computationally demanding since they often require large domain simulations and/or absorbing boundaries.

By itself, the finite element method (FEM) can be employed to model the foundation soil. Nevertheless, FEM computational efficiency is highly reduced due to the large number of elements required to provide an accurate soil representation – particularly when employing three-dimensional formulations. Thus, soil simulations via FE tend to restrict its number of elements and soil domain, and requires the inclusion of additional techniques to prevent wave reflection effect on its boundaries [28]. The perfectly matched layers (PML) provide a solution for this problem by simulating the absorbing domain and preventing wave's reflection at the boundaries of the model [55]. Therefore, the combination of both the FEM and the PML allow for the wave propagation behaviour representation and improves the computational efficiency.

Following this approach, the FEM-PML method can be combined with periodic strategies (i.e. DPM-FEM-PML) to further increase the efficiency of studying the ground-borne response. Fig. 8 shows a 3D reference cell, of domain $\widetilde{\Omega}$ and thickness $d$, with the railway track and ground components defined by the elastic domain $\widetilde{\Omega}_{FEM}$ and bounded by the PML domain $\widetilde{\Omega}_{PML}$ (i.e. $\widetilde{\Omega} = \widetilde{\Omega}_{FEM} \cup \widetilde{\Omega}_{PML}$).

### 3.4.1. PML stretching functions

The PML is a layer of elements with material properties similar to the elastic medium they bound or truncate. In addition, they can perfectly match the truncated medium by absorbing and attenuating outgoing waves from it [56]. The outgoing wave, travelling in the $s$ direction, is attenuated at a finite distance $\widetilde{H}_s$ within the PML domain $\widetilde{\Omega}_{PML}$ and is minimally reflected back toward the truncated domain $\widetilde{\Omega}_{FEM}$ from the outer fixed PML limit $\tilde{s}_t$ – see Fig. 9. Since the reflection of the wave is

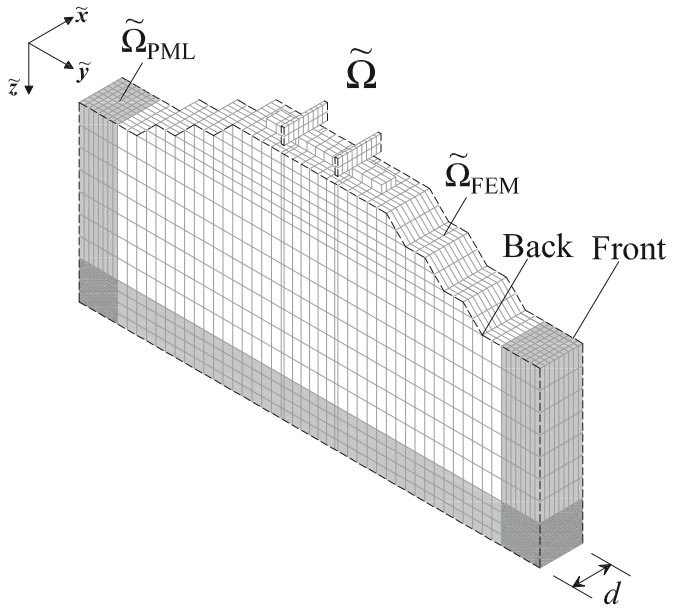


**Fig. 8.** 3D FE reference cell $\tilde{\Omega}_{FEM}$ bounded by PML layers $\tilde{\Omega}_{PML}$. Back and front boundaries in dashed lines.

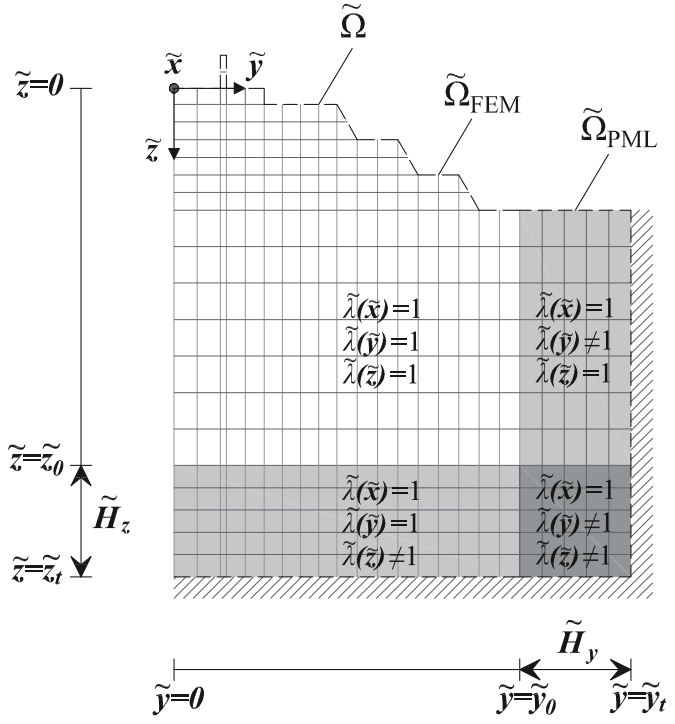


**Fig. 9.** Back face of reference cell $\tilde{\Omega}$ composed by linear $\tilde{\Omega}_{FEM}$ and PML $\tilde{\Omega}_{PML}$ domain. Limits and stretching functions $\tilde{\lambda}$ highlighted.

not significant, the PML is able to simulate unbounded domain [56,57].

The absorbing domain is defined through complex stretching coordinates $\breve{s}$, which allow for the artificial increment of the propagating wave attenuation [58]. Eq. (20) shows the stretching or new coordinate $\breve{s}$, derived from the stretching function $\tilde{\lambda}$, corresponding to each Cartesian coordinate within the reference cell domain $\tilde{s}$:

$$\breve{s}=\int_0^{\tilde{s}}\tilde{\lambda}(\tilde{s})\mathrm{d}\tilde{s}=\tilde{s}_0+\int_{\tilde{s}_0}^{\tilde{s}_t}\tilde{\lambda}(\tilde{s})\mathrm{d}\tilde{s},\ \begin{cases}\tilde{s}=\tilde{x},\tilde{y},\tilde{z}\\ \breve{s}=x,y,z\end{cases} \tag{20}$$

where $\tilde{s}_0$ and $\tilde{s}_t$ are the origin and end limits of the PML. Note that throughout $\tilde{\Omega}$, only $\tilde{\Omega}_{PML}$ is stretched and $\tilde{\Omega}_{FEM}$ remains unchanged – see Fig. 9. In addition, since the structure is assumed to be periodic in the longitudinal domain $\tilde{x}$, only $\{\tilde{s}\}=\{\tilde{y},\tilde{z}\}$ are stretched, as depicted in Eq. (21):

$$\breve{s}=\begin{cases}\breve{x}=\tilde{x}\\ \breve{y}=\int_0^{s}\tilde{\lambda}(\tilde{y})\mathrm{d}\tilde{y}\\ \breve{z}=\int_0^{s}\tilde{\lambda}(\tilde{z})\mathrm{d}\tilde{z}\end{cases} \tag{21}$$

Enforcement of $\tilde{\Omega}_{PML}$ is achieved through the same set of equations of motion defined for $\tilde{\Omega}_{FEM}$ (Eq. (14)). However, stretching coordinates $\{\breve{s}\}$ are used instead of the reference cell Cartesian coordinates $\{\tilde{s}\}$. Although different $\tilde{\lambda}$ formulations have been defined in the literature – see for instance Refs. [28,57–60], most stretching functions follow the formulation presented in Eq. (22):

$$\tilde{\lambda}(\tilde{s})=f_{\tilde{s}}^{e}(\tilde{s})-i\frac{f_{\tilde{s}}^{p}(\tilde{s})}{a_0} \tag{22}$$

where $f_{\tilde{s}}^{e}$ and $f_{\tilde{s}}^{p}$ are the polynomial functions that attenuate the evanescent and propagating waves inside the PML, respectively; and $a_0$ is a frequency dependent parameter related to the stretching function definition. This paper employs the stretching function proposed by Ref. [58], which defines the attenuation functions in terms of linear and quadratic polynomials with unit or zero values when computed within the FEM domain (Eq. (23)):

$$f_{\tilde{s}}^{e}(\tilde{s})=\begin{cases}f_{\tilde{s}_0}^{e}\dfrac{\bar{s}}{H_{\tilde{s}}};\tilde{\Omega}_{PML}=\left\{\tilde{s}_0<\tilde{s}\leq\tilde{s}_t\right\}\\ 1\quad;\tilde{\Omega}_{FEM}=\left\{\tilde{s}\leq\tilde{s}_0\right\}\end{cases}$$

$$f_{\tilde{s}}^{p}(\tilde{s})=\begin{cases}f_{\tilde{s}_0}^{p}\left(\dfrac{\bar{s}}{H_{\tilde{s}}}\right)^2;\tilde{\Omega}_{PML}=\left\{\tilde{s}_0<\tilde{s}\leq\tilde{s}_t\right\}\\ 0\quad;\tilde{\Omega}_{FEM}=\left\{\tilde{s}\leq\tilde{s}_0\right\}\end{cases} \tag{23}$$

$$a_0=k(k_1,\omega)=\sqrt{k_s^2-k_1^2} \tag{24}$$

where $f_{\tilde{s}_0}^{p}=2\pi/|k|$ and $f_{\tilde{s}0}^{e}=20$ are the parameters employed to adjust the amount of attenuation; $H_{\tilde{s}}$ and $\bar{s}=|\tilde{s}-\tilde{s}_0|$ are the layer thickness and the local Cartesian coordinates within $\tilde{\Omega}_{PML}$, respectively. In addition, $a_0$ or $k$ are the effective wavenumber for waves propagating along the cross-section (Eq. (24)). Note that to avoid mathematical problems, when $k_s^2=k_1^2$, the wavenumber is modified to $k_1=0.999k_1$. Similarly, $k_s=\omega/C_s$, is the variable depending on the angular frequency $\omega$ and the velocity of the shear wave $C_s$. Combining Eqs. (23)-(24) into Eq. (25), the latter becomes:

$$\tilde{\lambda}(\tilde{s})=\frac{2\pi}{|k|}\left(\frac{\bar{s}}{H_{\tilde{s}}}\right)-i\frac{20}{k}\left(\frac{\bar{s}}{H_{\tilde{s}}}\right)^2 \tag{25}$$

Depending on the PML region, the direction of the propagating waves varies (Fig. 9):

- $\tilde{\lambda}(\tilde{x}) = 1,\ \tilde{\lambda}(\tilde{y}) \neq 1,\ \tilde{\lambda}(\tilde{z}) = 1$; stretching coordinates in the $\tilde{y}$ direction only (i.e. side regions).
- $\tilde{\lambda}(\tilde{x}) = 1,\ \tilde{\lambda}(\tilde{y}) = 1,\ \tilde{\lambda}(\tilde{z}) \neq 1$; stretching coordinates in the $\tilde{z}$ direction only (i.e. bottom region).
- $\tilde{\lambda}(\tilde{x}) = 1,\ \tilde{\lambda}(\tilde{y}) \neq 1,\ \tilde{\lambda}(\tilde{z}) \neq 1$; stretching coordinates in the $\tilde{y}$ and $\tilde{z}$ directions (i.e. corner regions).

### 3.4.2. Equilibrium equations of motion

In the $\tilde{\Omega}_{PML}$, the partial derivatives with respect to the stretching coordinates (Eq. (26)) allows for the definition of the PML matrix of partial derivatives $[L_{PML}]$ (Eq. (27)):

$$\frac{\partial}{\partial \tilde{s}} = \frac{1}{\tilde{\lambda}(\tilde{s})}\frac{\partial}{\partial \tilde{s}};\quad \{s\} = \{x, y, z\} \tag{26}$$

$$[L_{PML}] = \left[\tilde{L}(\tilde{x}, \tilde{y}, \tilde{z})\right] = \begin{bmatrix} \partial/\partial\tilde{x} & 0 & 0 \\ 0 & \partial/\partial\tilde{y} & 0 \\ 0 & 0 & \partial/\partial\tilde{z} \\ 0 & \partial/\partial\tilde{z} & \partial/\partial\tilde{y} \\ \partial/\partial\tilde{z} & 0 & \partial/\partial\tilde{x} \\ \partial/\partial\tilde{y} & \partial/\partial\tilde{x} & 0 \end{bmatrix} \tag{27}$$

Note that in the direct periodic problem, the stretching coordinates are only present in the vertical $\tilde{y}$ and transversal $\tilde{z}$ direction; therefore, the partial derivatives with respect to the longitudinal axis $\tilde{x}$ remain unchanged in $[L_{PML}]$, i.e. $\tilde{\lambda}(\tilde{x}) = 1$ and $\partial/\partial\tilde{x} = \partial/\partial\tilde{x}$. Similar to the FEM case, the PML approach satisfies the differential system of equations (Eq. (9) and (10)). Thus, the reference cell stiffness and mass matrices in $\tilde{\Omega}_{PML}$, can be computed through Eqs. (27) and (28), respectively:

$$\left[K_{n=0}^{PML}\left(\tilde{x}, \tilde{\lambda}_{\tilde{y}}, \tilde{\lambda}_{\tilde{z}}\right)\right] = \int_{\tilde{x}}\int_{\tilde{y}}\int_{\tilde{z}} \tilde{\lambda}_{\tilde{y}}\tilde{\lambda}_{\tilde{z}}\left[\tilde{B}\right]^T[D]\left[\tilde{B}\right]d\tilde{x}d\tilde{y}d\tilde{z} \tag{28}$$

$$\left[M_{n=0}^{PML}\left(\tilde{x}, \tilde{\lambda}_{\tilde{y}}, \tilde{\lambda}_{\tilde{z}}\right)\right] = \int_{\tilde{x}}\int_{\tilde{y}}\int_{\tilde{z}} \tilde{\lambda}_{\tilde{y}}\tilde{\lambda}_{\tilde{z}}\left[\tilde{N}\right]^T\rho\left[\tilde{N}\right]d\tilde{x}d\tilde{y}d\tilde{z} \tag{29}$$

where $[K_{n=0}^{PML}]$ and $[M_{n=0}^{PML}]$ are the PML stiffness and mass matrices, respectively; and $\left[\tilde{B}\left(\tilde{x}, \tilde{\lambda}_{\tilde{y}}, \tilde{\lambda}_{\tilde{z}}\right)\right] = \left[\tilde{L}\left(\tilde{x}, \tilde{\lambda}_{\tilde{y}}, \tilde{\lambda}_{\tilde{z}}\right)\right]\left[\tilde{N}\left(\tilde{x}, \tilde{\lambda}_{\tilde{y}}, \tilde{\lambda}_{\tilde{z}}\right)\right]$ is the matrix of partial derivatives $\left[\tilde{L}\right]$ of the shape functions $\left[\tilde{N}\right]$. Since the PML domain is defined through complex stretching coordinates, all matrices in Eqs. (28)-(29) are also complex. Thus, $\left[\tilde{B}\right]^T$ and $\left[\tilde{N}\right]^T$ require the non-conjugate transpose instead of their conjugate transpose. Although in both cases, rows and columns are interchanged, in the former, the sign of the imaginary part remains unchanged, whereas, in the latter, they are the opposite. For instance, Eq. (30) shows the non-conjugate and conjugate transpose of matrix [A], $[A]^T$ and $[A]^{*T}$, respectively.

$$[A] = \begin{bmatrix} a_1 + ib_1 \\ a_2 + ib_2 \end{bmatrix} \Longrightarrow [A]^T = \begin{cases} [A]^T = [a_1 + ib_1 \quad a_2 + ib_2] \\ [A]^{*T} = [a_1 - ib_1 \quad a_2 - ib_2] \end{cases} \tag{30}$$

Eq. (31) describes the system of equations of motion in the total reference cell domain, in where the total dynamic stiffness matrix $[\tilde{D}_{n=0}^{FEM+PML}]$ is computed by properly assembling the matrices in both $\tilde{\Omega}_{FEM}$ and $\tilde{\Omega}_{PML}$ domains (Eqs. (32) and (33)).

$$[\tilde{D}_{n=0}^{FEM+PML}]\{\tilde{u}_{n=0}^{FEM+PML}\} = \{\tilde{F}_{n=0}^{FEM+PML}\} \tag{31}$$

$$[\tilde{D}_{n=0}^{FEM+PML}] = [\tilde{D}_{n=0}^{FEM}] + [\tilde{D}_{n=0}^{PML}] \tag{32}$$

$$\begin{aligned} \left[\tilde{D}_{n=0}^{FEM}(\tilde{x}, \tilde{y}, \tilde{z}, k_1, \omega)\right] &= \left[K_{n=0}^{FEM}(\tilde{x}, \tilde{y}, \tilde{z})\right] - \omega^2\left[M_{n=0}^{FEM}(\tilde{x}, \tilde{y}, \tilde{z})\right] \\ \left[\tilde{D}_{n=0}^{PML}(\tilde{x}, \tilde{y}, z, k_1, \omega)\right] &= \left[K_{n=0}^{PML}(\tilde{x}, \tilde{y}, z)\right] - \omega^2\left[M_{n=0}^{PML}(\tilde{x}, \tilde{y}, z)\right] \end{aligned} \tag{33}$$

where $[K_{n=0}^{FEM,PML}]$ are complex stiffness matrices accounting for the hysteretic damping model.

## 4. Model verification

This section presents a numerical verification that demonstrates the accuracy of the DPM formulation. The method is employed to approximate the dynamic response of a structure and its wave propagation effect, thus confirming that the 3D DPM-FEM can be coupled with PML (i.e. 3D DPM-FEM-PML). This verification considers the example described in Ref. [39], which uses the fully analytical solution proposed by Tadeu and Kausel [59].

Fig. 10 shows the geometry of the 3D DPM reference cell: a 3 m × 3 m FEM mesh bounded by a PML layer of 1 m of width in the vertical and transversal directions, both with thickness $d = 6 \times \Delta x$, where $\Delta x = 0.1$ m is the size element in the periodic direction $x$. Also, the reference cell is defined by linear brick elements, 9600 elements with 11767 nodes in total, described by hysteretic damping in the frequency domain. The symmetry of the structure is exploited, therefore only half of the domain is modelled. Regarding the boundary conditions, constraints are applied at the ends of the PML domains (black markers) and the symmetry axis (blue markers). In addition, the ground domain is constrained longitudinally and transversally at the top (red markers), i.e. in the $x$ and $y$ direction, respectively.

This domain is subject to a stationary force $F = Pe^{i\omega t}$ of magnitude

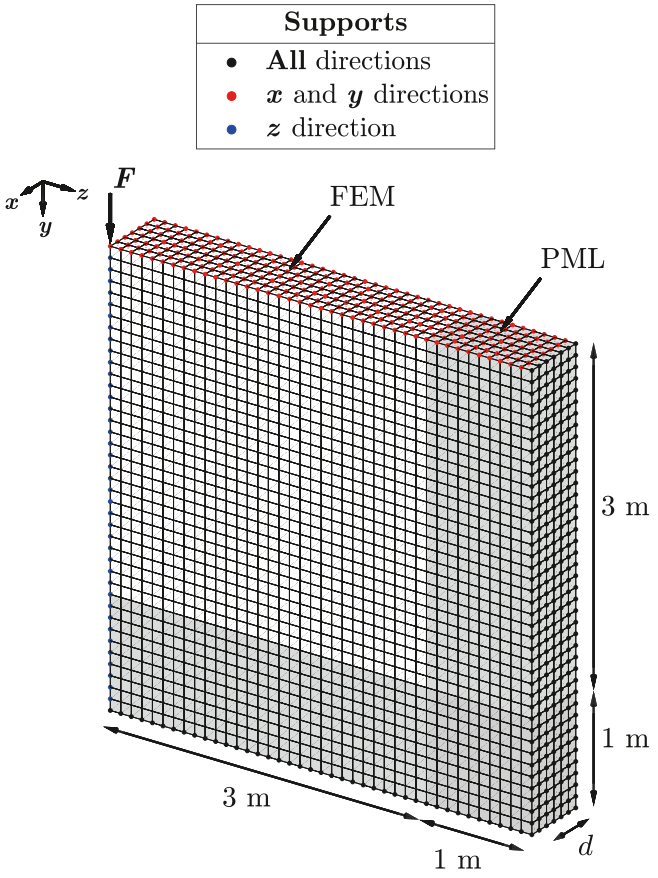


**Fig. 10.** 3D DPM reference cell.

$P = 0.25$ N applied at the axis origin ($x = y = z = 0$ m) and excited by two frequencies $\bar{f} = [10, 75]$ *Hz*, where the angular frequency is $\varpi = 2\pi\bar{f}$, and $t$ is the time. Regarding the material properties, the soil has a Young's modulus $E = 80$ MPa; velocity of the shear and dilatational waves $C_s = 126.5$ m/s and $C_p = 219.1$ m/s, respectively; Poisson's coefficient $\nu = 0.25$; density $\rho = 2000$ kg/m$^3$; and loss factor $\eta = 0.002$.

The vertical surface displacements are computed along the transversal direction (i.e. $x = y = 0$ m) at three dimensionless wavenumbers $\bar{k}_1 = [0.5, 1.0, 1.5]$, where the wavenumber is defined by $k_1 = \bar{k}_1 \varpi / C_s$. Figs. 11 and 12 compares the real and imaginary components of the response computed via the periodic and analytical solution at 10 *Hz* and 75 *Hz*, respectively. In both cases, the periodic model uses the stretching function $\tilde{\lambda}(\bar{s})$ defined in **Eq. (25)**. It can be seen that periodic results yield a good approximation to the analytical solution for $\bar{k}_1 = [0.5, 1.5]$. However, small discrepancies are evident at $\bar{k}_1 = 1.0$ due to the numerical inaccuracy in the periodic method when $k_1 = \varpi / C_s$. Overall, results confirms the accuracy of the DPM-FEM-PML when simulating the ground behaviour and its wave propagation effect.

Finally, it is important to highlight that since the material and geometrical properties of the structure are continuous along the periodic direction (longitudinal axis $x$), the thickness of the reference cell in the DPM can be reduced from $d = 6 \times \Delta x$ to a single value $d = \Delta x$, i.e. from 11767 to 3362 nodes. This domain reduction produces similar results to the obtained in Figs. 11 and 12 and allows for further optimisation of the periodic simulation.

## 5. Model refinement for receptance applications

The receptance calculation models presented in the literature often make assumptions regarding the track to improve computational efficiency. One common assumption is the track support can be modelled as a rigid boundary condition rather than a flexible condition representative of the underlying earthworks. Another is that symmetry can be assumed along the track centreline, meaning both rails are excited rather than one, which is unlikely to be the case when field testing. This section investigates the validity of these two assumptions. It is shown that large errors at frequencies up to 450 *Hz* are introduced if the track support conditions are not adequately considered. Similarly, errors are introduced up to approximately 800 *Hz* when comparing symmetrical and non-symmetrical loading.

### 5.1. Modelling parameters

The DPM is used for all receptance calculations. Table 2 shows the characteristic or base parameters, while Appendix A shows all additional properties. Note that the selected base permutation corresponds to a stiff track supported by well-compacted earthworks, which is characteristic of a modern high-speed track. Also, under-sleeper pad (USP) and the presence of the embankment are ignored during model refinement.

All components are defined using linear brick elements (8-node solid elements) with hysteretic damping – as described in **Eq. (8)**. Fig. 13 shows the 3D view of the reference cell mesh with thickness $d$, defined according to the sleeper spacing.

The reference cell is subject to a stationary force of magnitude $F = 1$ N excited at frequency $\omega$, which is evenly applied on top of both rails above the sleeper support ($x = d/2$) – see **Eqs. (11)** and (12). The vertical deflection is computed at different track positions, initially in $(k_1, \omega)$ domain and later transformed back to $(x, \omega)$. Fig. 14 shows the position of the excitation $F$ and the observation points where the response is obtained:

(1) rail above sleeper – $u(x = d/2,\ y = y_{\text{rail}},\ z = \pm z_{\text{rail}})$,
(2) rail at mid-span – $u(x = 0,\ y = y_{\text{rail}},\ z = \pm z_{\text{rail}})$,
(3) sleeper shoulder – $u\left(x = d/2,\ y = y_{\text{sleeper}},\ z = \pm z_{\text{sleeper},1}\right)$, and

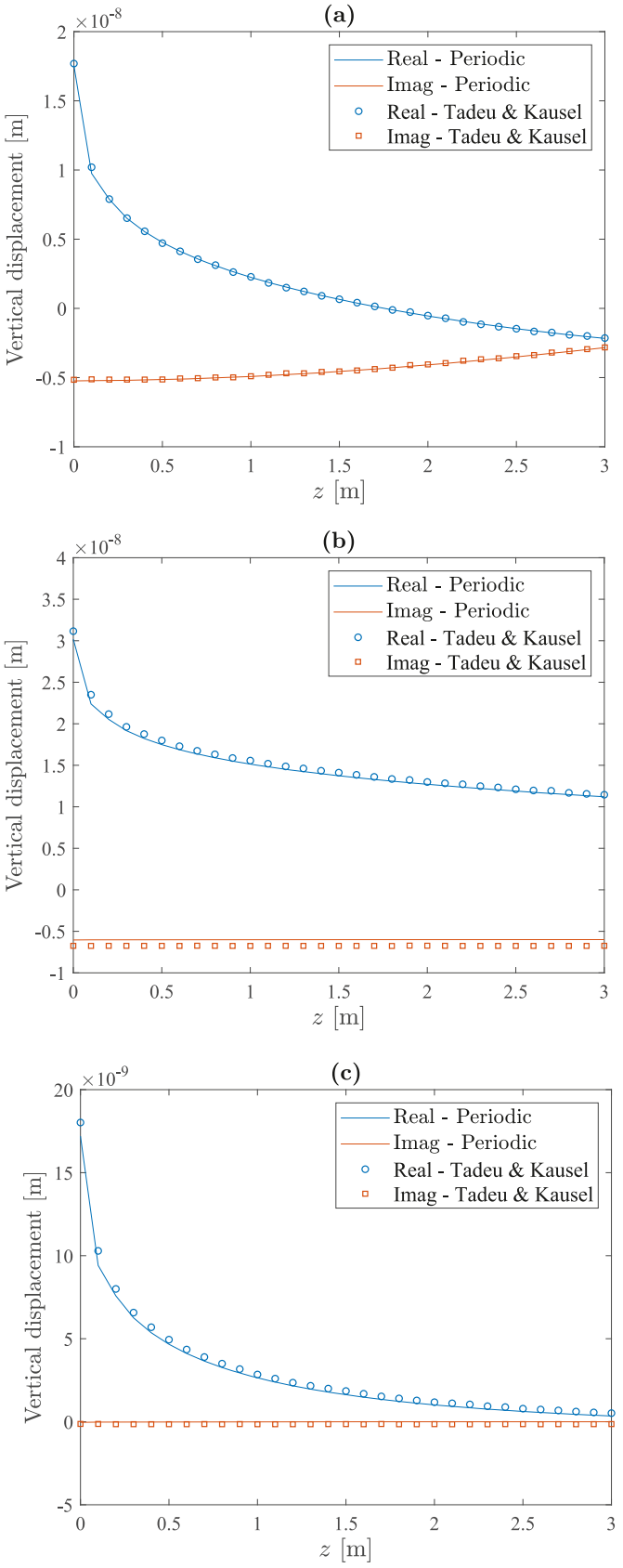


**Fig. 11.** Vertical deflection at $\bar{f} = 10$*Hz*: (a) $\bar{k}_1 = 0.5$, $\bar{k}_1 = 0.5$, (b) $\bar{k}_1 = 1.0$, and (c) $\bar{k}_1 = 1.5$.

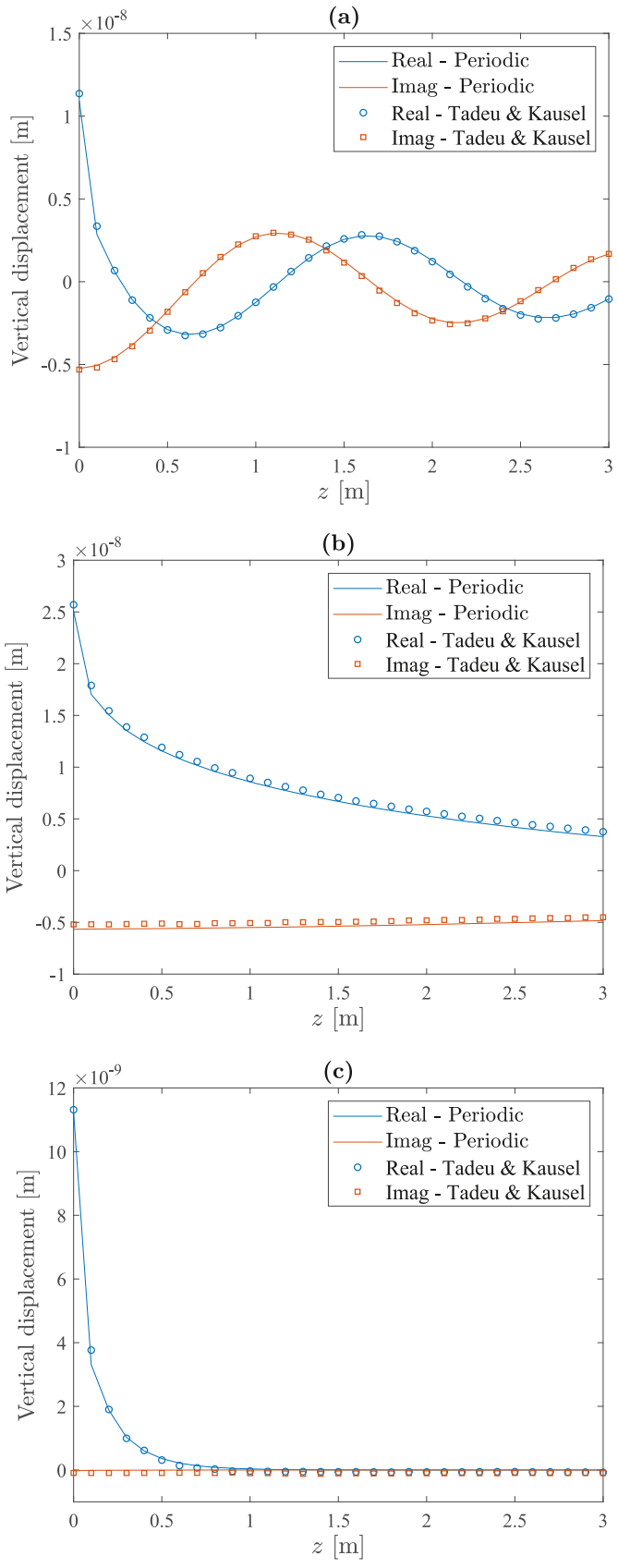


**Fig. 12.** Vertical deflection at $\bar{f} = 75Hz$: (a) $\bar{k}_1 = 0.5$, $\bar{k}_1 = 0.5$, (b) $\bar{k}_1 = 1.0$, and (c) $\bar{k}_1 = 1.5$.

**Table 2**
Main track parameters – Base permutation.

| Component | Parameter | | Value |
|---|---|---|---|
| Track | $l_0$ | Gauge | 0.7175 m |
| Reference cell | d | Length | 0.6 m |
| Rail | – | Section | CEN60/60E2 |
| Railpad | $E_{rp}$ | Young's modulus | 200 MPa |
| Sleeper | – | Material | Concrete |
| USP | $l_{yusp}$ | Depth | 0 m |
| Ballast | $E_b$ | Young's modulus | 220 MPa |
| | $l_{yb}$ | Depth | 0.3 m |
| Sub-ballast | $l_{ysb}$ | Depth | 0.2 m |
| Embankment | $l_{ye}$ | Depth | 0 m |
| Subgrade | $E_{sg}$ | Young's modulus | 80 MPa |

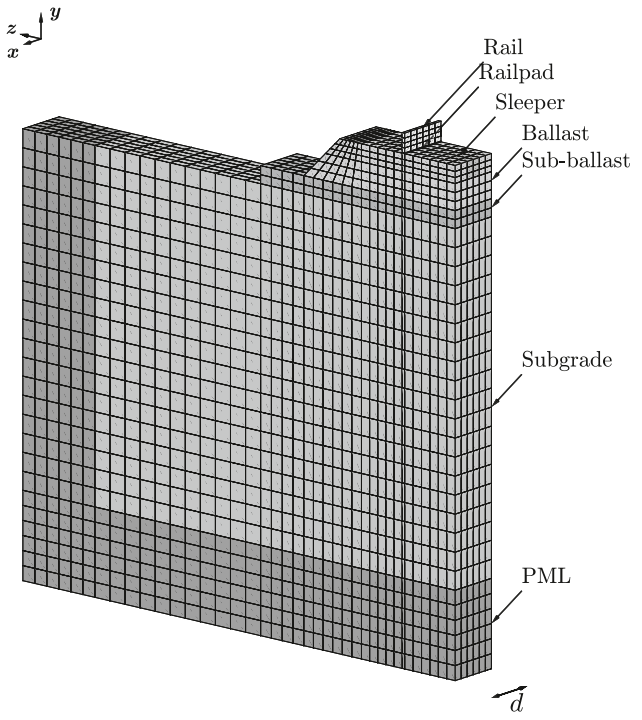


**Fig. 13.** Base permutation reference cell mesh 3D view. Only half-track shown for visibility purposes.

(4) sleeper centre – $u\left(x = d/2,\ y = y_{\text{sleeper}},\ z = \pm z_{\text{sleeper},0}\right)$,

in where $y_j$ and $z_j$ are the vertical (top) and transversal coordinates of $j = \text{rail}, \text{sleeper}$. Note that $z = z_{\text{sleeper},0}$ describes the centre of mid-span coordinate of the sleeper. In contrast, $z = z_{\text{sleeper},1}$ corresponds to the mid coordinate between the sleeper end and the rail. Additionally, only in case (1) the response is a receptance – since the deflection is obtained at the same coordinate as the excitation. In contrast, in cases (2), (3) and (4), the result is a transfer function (or a cross-receptance) since both coordinates differ.

The frequency range of study is $f = [0 - 1600]\,Hz$, while the wavenumber sampling is $k_1 = [-k_{1,max} : k_{1,max}/2048 : k_{1,max}]$, where $k_{1,max} = 20\ \text{rad/m}$. This sampling is chosen because it is sufficient to capture the response from both the track and the ground. Regarding discretisation, element size is, $\Delta x = d/6$, where $d$ is cell thickness.

### 5.1.1. *Flexible vs rigid trackbed support*

To study the support conditions, the frequency responses of a track resting on a semi-infinite ground and on a rigid support are compared – see Fig. 15. In both cases, base parameters are employed and results are

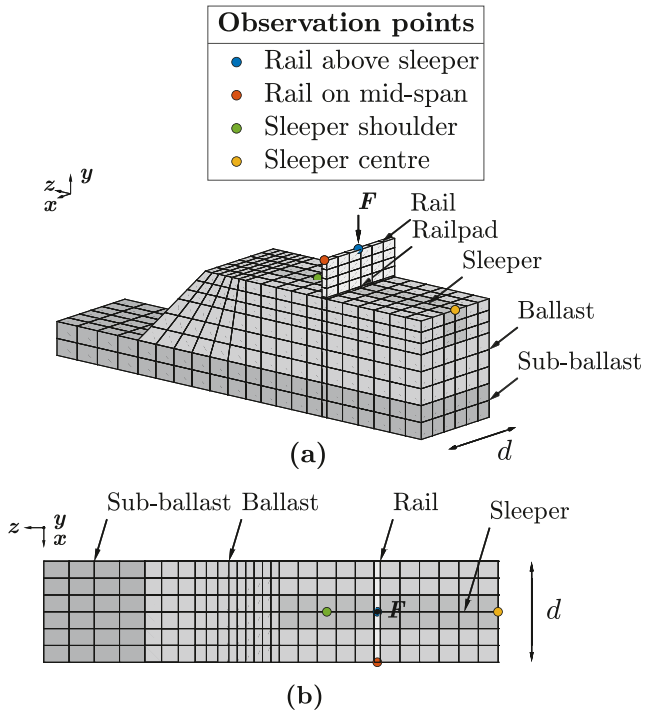


**Fig. 14.** Excitation and observation point locations within the ballasted track model: (a) 3D view and (b) birdseye view. Subgrade layer omitted and only half-track shown for visibility.

shown in terms of absolute vertical deflections at different points on the rail and the sleeper – see Fig. 14.

Fig. 16 illustrates the absolute deflection computed in a track resting on a subgrade or flexible support (TS) and on a rigid support (TR). Results computed at the rail above sleeper and at mid-span – see Fig. 16(a), show that the maximum deflection is obtained at low frequencies: at 0 to 50 *Hz* in TS and at 130 *Hz* in TR. This behaviour is attributed to soft lower components supporting much stiffer upper layers. In TS model, the maximum response corresponds to the subgrade $f_{\text{subgrade}}$. This additional component leads to wave-propagation effect, magnifying the response below 50 *Hz* and making it challenging to identify $f_{\text{full-track}}$, the frequency of resonance related to the lower-track layers (i.e. ballast and sub-ballast), above this frequency. Alternatively, in TR model, the maximum occurs at $f_{\text{full-track}}$ and $f_{\text{subgrade}}$ is not visible due to the absence of the subgrade.

Above these frequencies, the amplitude decays, reaching a low region between $50 - 180$ *Hz* and $160 - 220$ *Hz* in TS and TR, respectively. In the latter case, the minimum is observed at a lower sharp peak around 180 *Hz* and can be interpreted as $f_{\text{sleeper}}$. In contrast, this region is not clearly delineated in the former case, and its minimum is not prominent. This occurs because of the wave propagation effect, which makes it challenging to identify $f_{\text{sleeper}}$.

After this low region, the amplitude of the response increases in both models and two upper peaks are observed: at 250 *Hz* and 400 *Hz* for the rigid support, and 320 *Hz* and 440 *Hz* in the subgrade support model. Note that the second peaks are close to convergence, indicating that the subgrade impact has decreased. Then, above 440 *Hz*, both models overlap and the response is governed by upper track components. Similarly, new peak occurs at 730 *Hz* at both observation points. Although no evident difference between these peaks, they are all associated to $f_{\text{rail}}$. Note that both curves experience a rapid decay above 800 *Hz*. This behaviour is attributed to the frequency of resonance of the rail, $f_{\text{pin-pin}}$, which is not captured in the frequency range displayed in

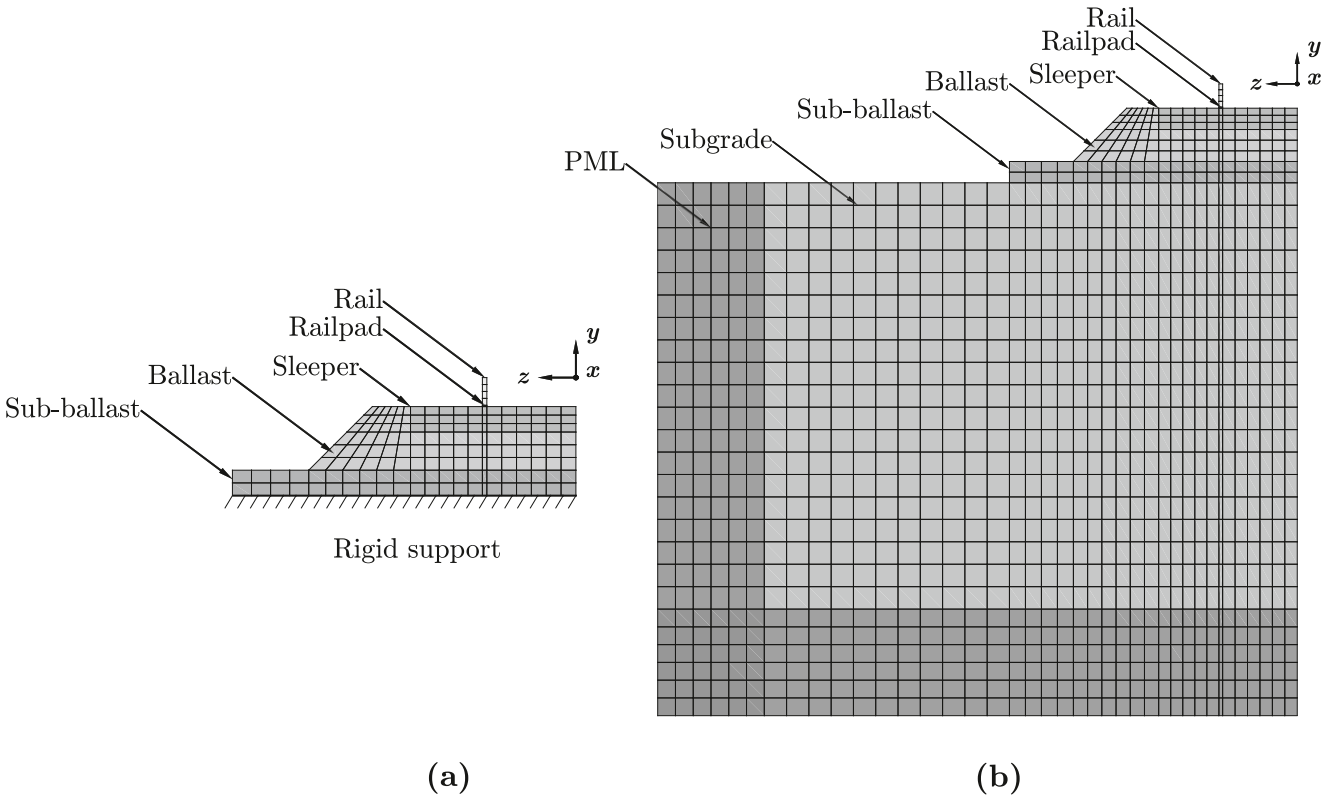


**Fig. 15.** Ballasted track model support conditions: (a) rigid trackbed, and (b) flexible trackbed. Half-track transversal view shown for visibility.

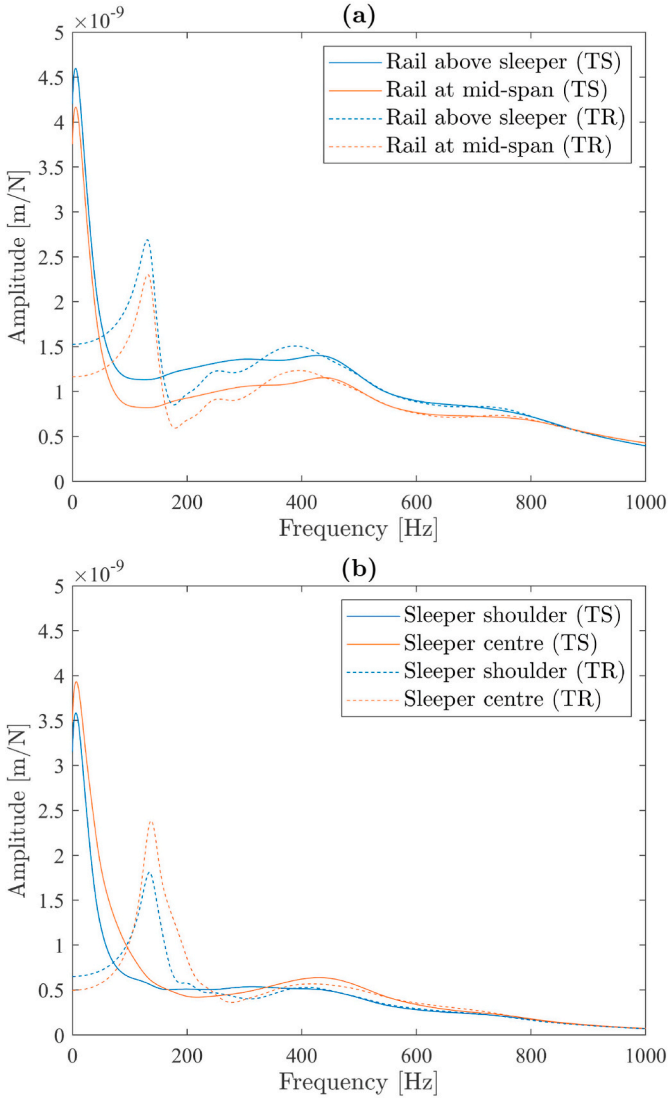


**Fig. 16.** Deflections due to a track on subgrade (TS) and a track on rigid support (TR) at: (a) at rail above sleeper and rail at mid-span, and (b) sleeper shoulder and sleeper centre.

Fig. 16.

Alternatively, Fig. 16(b) shows the absolute deflection at the shoulder and centre of the sleeper. Again, the greatest response occurs at lower frequencies: at $f_{\text{subgrade}}$ and $f_{\text{full-track}}$ in TS and TR, respectively. After these frequencies, all curves decay reaching their minimum between $50-250\,Hz$ in TR and $200-350\,Hz$ in TS. The low region is clearly defined in the latter. However, this range differs to the displayed at the rail observation points in Fig. 16(a), and the minimum at the sleeper points occurs at a higher frequency that in the rail case. This behaviour is typical of the vibration mode related to $f_{\text{sleeper}}$, in where the sleeper's deflection is larger than the rail.

Regarding the subgrade case, its low region is not well defined due to the subgrade properties. This behaviour and range are consistent with results obtained at the rail observation points (see Fig. 16(a)), indicating that the sleeper follows a behaviour close to that of the rail. This can be explained by a combination of factors, such as a soft supporting subgrade, a low sleeper mass, and a strong connection between the rail and the sleeper [16].

Next, an upper peak develops around $440\,Hz$ where both models converge. Above this frequency, all curves decay, illustrating the reduced of the sleeper and the rail and railpad track dominance. Regarding the observation point, both support models show that the sleeper at mid-span experiences a greater amplitude compared to that on support. This behaviour can be explained by the bending effect of the sleeper.

Figs. 17–19 compare the vibration modes due to different support conditions according to the resonant frequencies identified in Fig. 16. To improve visibility, only 11 track cells are illustrated (i.e. $n = -5:5$), and the railpad height and all deflection values have been magnified (by a percentage increment of 800% and a factor of $1E3$, respectively). Fig. 17 shows the absolute deformation of (a) a track resting on rigid support excited at $130\,Hz$, (b) a zoomed view of a track on a flexible support excited at $6\,Hz$, and (c) a full view of a track on a flexible support excited at $6\,Hz$. The first vibration mode in (a) corresponds to $f_{\text{full-track}}$, while the response at (b) and (c) is related to $f_{\text{sub-grade}}$. Although in all cases the track components move in phase with a broad bending wave-shape, the wave propagation effect of the subgrade magnifies the response, resulting in a larger deformation in (b) and (c) compared to (a).

Fig. 18 presents the absolute deformation related to $f_{\text{sleeper}}$. Fig. 18(a) shows the response at $180\,Hz$ in the rigid-support case, in where the rail deflection is much lower than the sleeper. Since identifying $f_{\text{sleeper}}$ in a track on subgrade model is challenging, deflections at two frequencies are plotted: $100\,Hz$ and $130\,Hz$, as seen in Fig. 18(b) and (c) respectively. These values lie within low frequency range described in Fig. 16. At $100\,Hz$, the track components move in phase with both the rail and

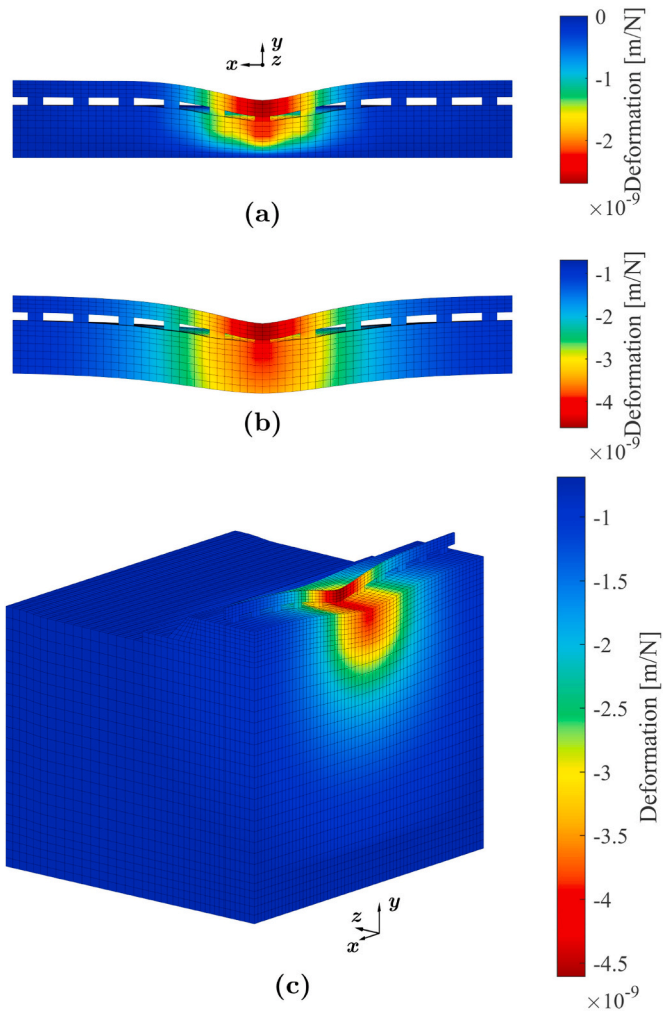


**Fig. 17.** Vertical deflections of: (a) track on rigid support excited at $130\,Hz$ – longitudinal view, (b) track on subgrade support excited at $6Hz$ – zoomed longitudinal view, and (c) track on subgrade support excited at $6\,Hz$ – 3D view.

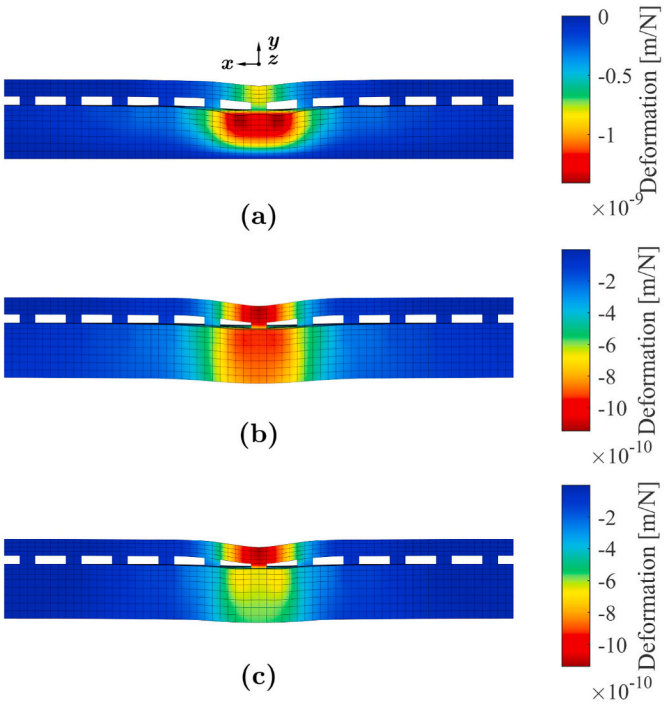


**Fig. 18.** Vertical deflections of: (a) track on rigid support excited at 180 *Hz*, (b) track on subgrade support excited at 100 *Hz* – zoomed view, and (c) track on subgrade support excited at 130 *Hz* – zoomed view. Longitudinal views.

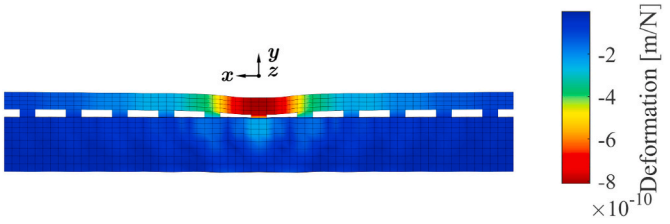


**Fig. 19.** Vertical deflections due to an impulse excited at 730 *Hz* – zoomed view. Longitudinal view.

the sleeper experiencing a large deflection. In contrast, at 130 *Hz*, the sleeper displays minimal movement relative to the rail. Overall, (b) shows that the sleeper follows a behaviour similar to the rail. In contrast, (c) illustrates how the sleeper effect decreases with frequency.

Alternatively, Fig. 19 illustrates the track deflections at $f_{\text{rail.2}} = 730\ Hz$, where the rail moves in anti-phase with the supporting track layers. Note that although $f_{\text{rail.2}}$ lies in the upper mid-range, the rail deflection and response propagation within the lower track layers are still visible at this frequency.

Fig. 20 compares the difference in amplitude between both support conditions at all observation points. Results show that the maximum difference is found at lower frequency ranges, within $f_{\text{sub-grade}}$ range, where an error of approximately 80% occurs at 0 *Hz*. This high error occurs due to the absence of $f_{\text{subgrade}}$ under rigid support conditions. Similarly, the subgrade presence amplifies the response, making identifying $f_{\text{full-track}}$ and $f_{\text{sleeper}}$ challenging. This behaviour explains the maximum error of 300% at around 130 *Hz*. The error rapidly decays with frequency, reaching an average of 30% between 200 – 440 *Hz*. This range corresponds to the frequencies of resonance of the rail ($f_{\text{rail}}$) occurring in both models. Above 440 *Hz*, all observation points yield an error of approximately 10%. This low error is expected since both models converge at higher frequencies. Regarding the observation points, the maximum error is obtained at the sleeper. This occurs due to

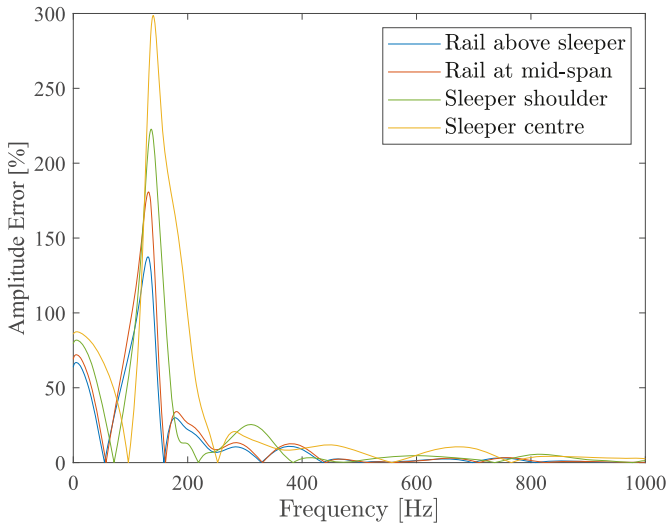


**Fig. 20.** Amplitude error between track on subgrade and track on rigid support model at different observation points.

the subgrade properties, which greatly influence the lower-track layers, including the sleeper. In contrast, the overall minimum is observed at the rail on support, where the excitation is applied.

### 5.1.2. *Symmetry boundary conditions*

Numerical simulations of track receptance typically assume the track can be modelled using a centreline symmetry condition. Although this reduces computation requirements, it means both rails must be excited in an identical manner. In contrast, in-situ receptance test configurations excite a single side of the structure, thus making the problem inherently non-symmetric. In order to study the effect of this symmetry assumption and its effect on track bending modes, a full-track model is excited in two different ways:

(1) symmetric loading, where $F_1 = F_2 = 0.5$ N, and
(2) non-symmetric loading, where $F_1 = 0.5$ N and $F_2 = 0$ N

In Configuration (1), a full-width track is excited by identical forces on both sides of the track. This is the case of a track centreline symmetry condition, as commonly used in numerical simulations to approximate the response due to rolling stock excitation. In contrast, configuration (2) is used to excite only one side of the track, as commonly performed during receptance field-testing that excites a single side of the track. Fig. 21 illustrates the reference cell with the observation and excitation points arrangement used to study symmetry conditions. Note that for comparison purposes, configuration (2) sets $F_1 = 0.5$ N.

However, for a closer approximation to in-situ receptance conditions, $F_1$ should be 1.0 N. Additionally, considering the geometrical symmetry of the structure (symmetric boundary conditions and linear material properties), it is possible to approximate case (2) by combining two symmetric models subject to:

(a) symmetric loading, where $F_1 = F_2 = 0.25$ N, and
(b) anti-symmetric loading, where $F_1 = 0.25$ N and $F_2 = -0.25$ N.

Fig. 22(a) and (b) show the absolute deflection at the rail above the sleeper and mid-span, and at the shoulder and centre of the sleeper, respectively. In both cases, symmetric (Symm) and non-symmetric (NSymm) excitation are compared. Fig. 22(a) shows that in the case of symmetric conditions, the structure is equally loaded and provides similar results on both sides. Due to this behaviour, only a single side of the structure response is presented in Symm case. Alternatively, in NSymm case, the response at the loaded (Load) and unloaded (ULoad)

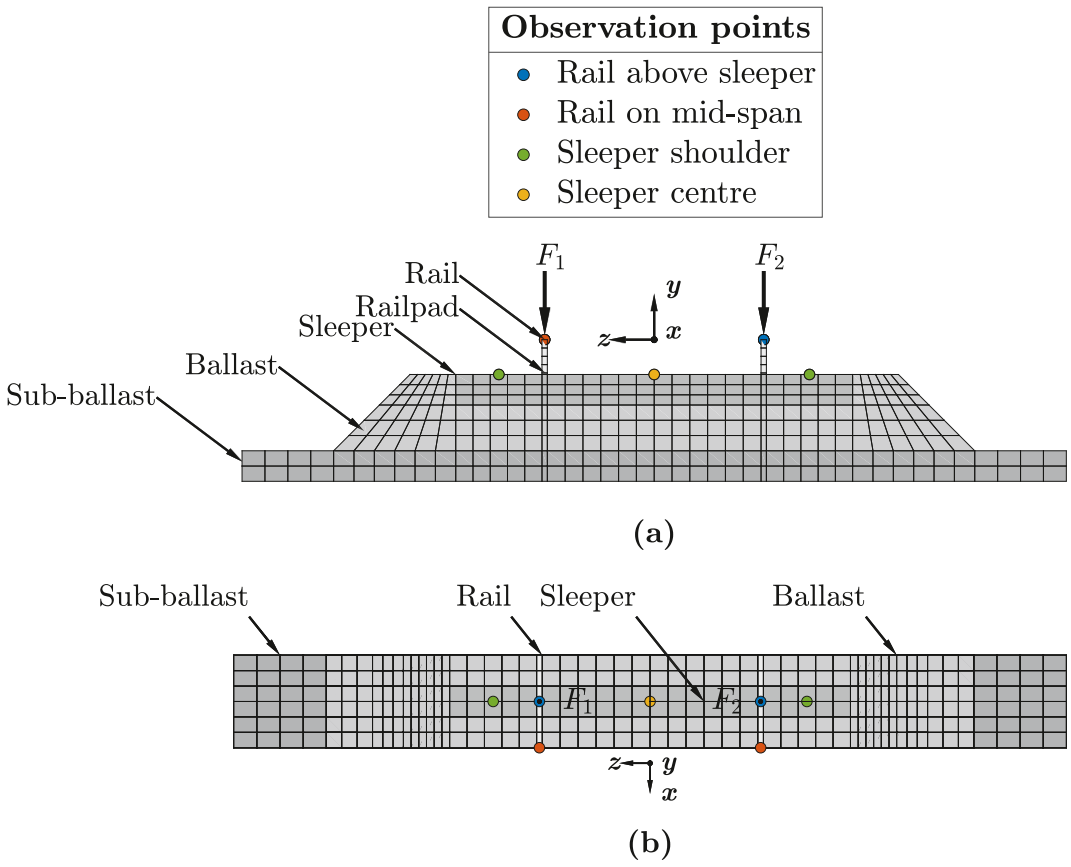


**Fig. 21.** Excitation and observation point locations within the full-track model: (a) transversal view and (b) birdseye view. Subgrade layer omitted for visibility.

sides differ, indicating non-symmetric deformations, with the maximum response obtained at Load-side.

It can be seen that the overall maximum occurs when both sides of the track are equally excited. This difference is particularly evident between $0-50$ *Hz*, i.e. around $f_{\text{sub-grade}}$. Between $50-180$ *Hz*, results shift and the maximum is obtained in the NSymm case at both observation points. At this frequency range, the response of the sleeper ($f_{\text{sleeper}}$) is more rigid in NSymm than Symm.

Above 180 *Hz*, four main frequencies are identified: $f_{\text{rail},0} = 320$ *Hz*, $f_{\text{rail},1} = 440$ *Hz*, $f_{\text{rail},2} = 600$ *Hz*, and $f_{\text{rail},3} = 730$ *Hz*. Excluding the peak at $f_{\text{rail},0}$, all frequencies of resonance at $f > 180$ *Hz* differ in both models and NSymm frequencies values are higher than those obtained in Symm. Also, although only Load-side is excited, the response propagates to the opposite ULoad-side, resulting in small yet significant deformations on the latter. However, between $180-400$ *Hz* and above 800 *Hz*, ULoad-side's contribution reaches its minimum, explaining the convergence of both models at these ranges.

Regarding the sleeper's results – see Fig. 22(b), it is seen that as the sleeper centre is a unique point corresponding to the geometric centre of the track, a single curve is retrieved for this observation point in the NSymm-model. Thus, only for the sleeper shoulder, results are presented for both loaded (Load) and unloaded (ULoad) sides. Similar to the rail results (Fig. 22(a)), sleeper's deflections obtained with Symm-model are symmetric, thus indicating symmetric bending modes. Alternatively, Load-side results differ from ULoad in NSymm, thus sleeper bending models are non-symmetric in this case.

It can be seen that, below 600 *Hz*, the overall maximum is found with Symm-model at both observation points. However, both models converge above this frequency at the sleeper shoulder, and after 1000 *Hz* at the sleeper centre. Again, both models converge when NSymm – ULoad contribution is minimum. However, as the result at sleeper centre is only provided by a single point, results converge at a higher frequency than the sleeper shoulder case.

Although the excitation is non-symmetric in NSymm, its structure (including its boundary conditions and geometrical and linear material properties) is fully-symmetric. Thus, combination of Load- and ULoad-side at each observation point in NSymm can approximate the fully symmetric model. Fig. 23 compares the total response due to the non-symmetric model ($\text{NSymm}_{\text{tot}}$) with the corresponding symmetric results (Symm). However, since the sleeper centre response at the non-symmetric model retrieves a single value, the corresponding $\text{NSymm}_{\text{tot}}$ result is obtained by doubling its response.

Fig. 24 compares the difference in amplitude between symmetric and non-symmetric conditions models at all observation points. Results show that symmetric conditions induce moderate errors ($\approx 20\%$) at around $0-20$ *Hz*, $60-100$ *Hz*, $420-520$ *Hz* and $570-700$ *Hz*. These ranges correspond to the frequencies of resonance $f_{\text{subgrade}}$, $f_{\text{sleeper}}$, $f_{\text{rail},1}$ and $f_{\text{rail},2}$, respectively. In contrast, lower errors $< 20\%$) are observed at the remaining frequencies, where both models converge. Note that as the sleeper centre response in the non-symmetric model is half the symmetric case, it will lead to a constant error of approximately 100%, thus, the error at this observation point is not included in Fig. 24.

Figs. 25–28 compare the absolute track deflections caused by symmetric and non-symmetric loading, when excited at various frequencies. Three-dimensional and transverse views results are employed to highlight the transversal bending modes at the upper track layers. Firstly, Fig. 25 presents the track deformation at 6 *Hz*. At this frequency, the response is mainly affected by the subgrade properties and the symmetric model yields larger deflections than the non-symmetric case. The maximum deformation occurs at the rail, the point where the force is applied, and its effect propagates in all directions within the track, with a considerable contribution in the sleeper below. In the symmetric case, the force is evenly distributed along the track, resulting in a symmetric bending mode. In contrast, the transversal bending mode of the track is

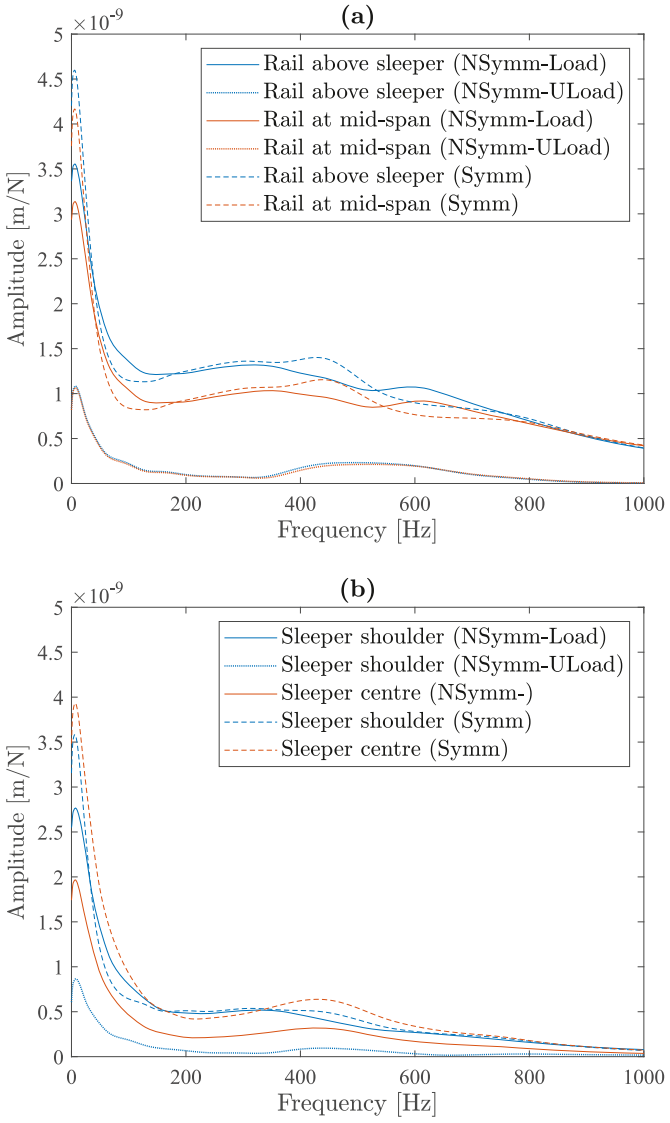


**Fig. 22.** Deflections at: (a) rail above sleeper and at mid-span, and (b) sleeper shoulder and centre. Full-track model: non-symmetric loaded side (NSymm – Load), non-symmetric unloaded side (NSymm – ULoad), and fully-symmetric loaded (Symm).

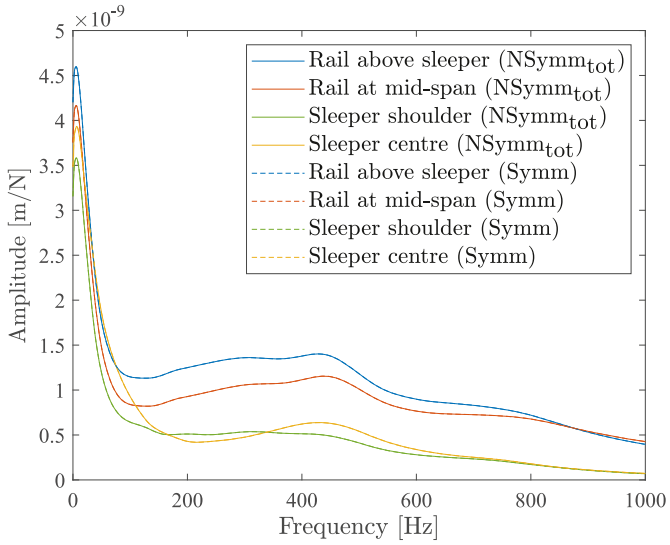


**Fig. 23.** Deflections at different observation points of a full-track model: non-symmetric total (NSymm$_{tot}$), and fully-symmetric (Symm).

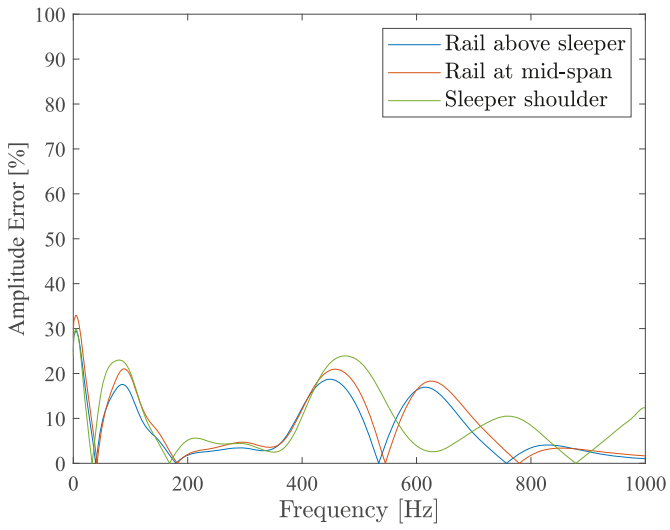


**Fig. 24.** Amplitude error between symmetric and non-symmetric loaded model at different observation points – track on subgrade support.

non-symmetric in the non-symmetric case, and its loaded side experiences the greatest deflection. Overall, the large response in both cases is due to the magnification effect resulting for the wave propagation effect at low frequencies.

Fig. 26 illustrates that at 130 *Hz*, the maximum is achieved with the non-symmetric configuration. Because the influence of the subgrade diminishes with frequency, the propagation of the response within the track is less significant at 130 *Hz* than at 6 *Hz* (Fig. 25).

Fig. 27 shows the absolute deformation at 320 *Hz*. Both results present similar magnitudes, with the symmetric case displaying a slightly higher value. This similarity is responsible for the near-undeformed deformation on the unloaded side of the non-symmetric model. It can be observed that the propagation of the response within the lower-track layers is lower at 320 *Hz* than at 130 *Hz* (see Fig. 26). This is because as frequency increases, the track component's effect on the response increases while the subgrade's effect decreases.

Alternatively, results computed at 440 *Hz* – see Fig. 28, show that the symmetric model provides a greater deformation compared to the non-symmetric. The difference between both models is also presented on the unloaded side of the non-symmetric case, which is considerable and larger than the obtained in the quasi-undeformed result at 320 *Hz* (see Fig. 27). Similarly, the deformation is concentrated on the upper-track layers, accounting for their relevance at higher frequencies.

Finally, it is evident that symmetry conditions have an effect on receptance results. In a symmetrical configuration, two forces of equal magnitude are applied on two opposite positions, resulting in a response that propagates evenly along the track to the ground support and symmetric transversal bending modes. In contrast, in a non-symmetrical configuration a single impulse leads to non-symmetric bending modes, where the maximum response, occurring at the loaded side, gradually decreases as it extends to the opposite and unloaded side. In addition, results show non-symmetric conditions lead to lower deflections and lower frequencies of resonance compared to the symmetric case. Thus, to realistically approximate receptance field tests, a full-track model with non-symmetric conditions (with $F_1 = 1$ N and $F_2 = 0$ N) is considered hereafter. Regarding the support conditions, the subgrade component is considered at low- and mid-frequency ranges while disregarded at higher-frequency, ranges for simplicity purposes.

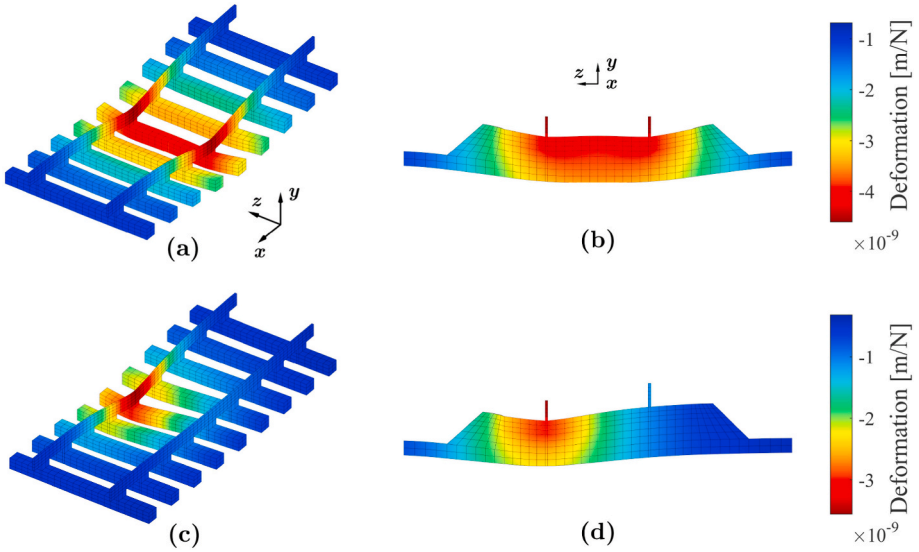


**Fig. 25.** Absolute track deformation at 6 *Hz*: (a) symmetric force model 3D view, (b) symmetric force model transversal view, (c) non-symmetric force model 3D view, and (d) non-symmetric force model transversal view. Lower components removed for visibility.

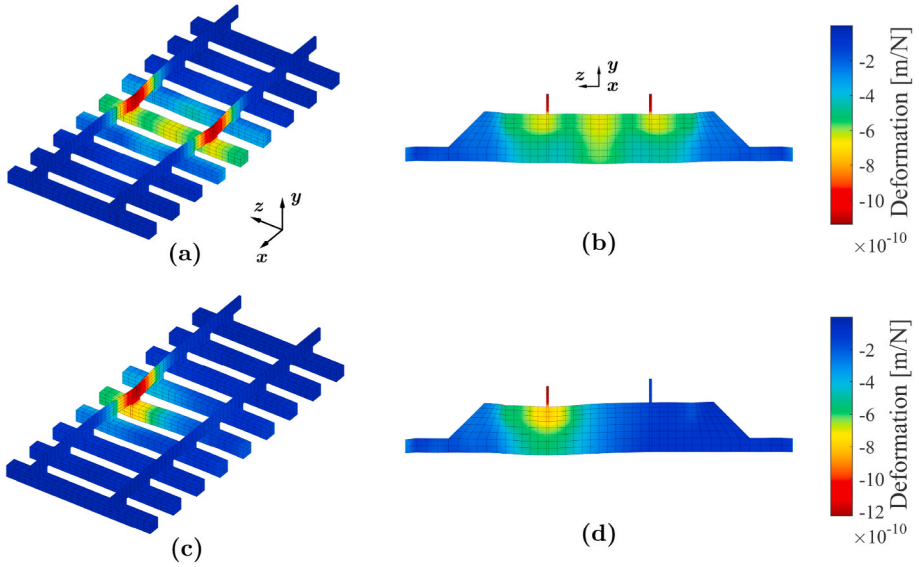


**Fig. 26.** Absolute track deformation at 130 *Hz*: (a) symmetric force model 3D view, (b) symmetric force model transversal view, (c) non-symmetric force model 3D view, and (d) non-symmetric force model transversal view. Lower components removed for visibility.

## 6. Sensitivity study

A sensitivity study is performed to study the geometric and material properties of the track. Appendix A presents the properties of each track component while the track properties defined in Table 2 are the base parameters. Table 3 highlights the base permutation and the 17 combinations grouped according to the characteristic parameters related to each component. Fig. 29 shows the 3D view of the reference cell mesh with all studied components. Note that the base simulation did not include under-sleeper pads (USP) or an embankment. Using the findings related to model design from the previous section, the full track width is modelled (i.e. no symmetry condition), supported by an infinitely deep soil medium.

### 6.1. Rail

Fig. 30 presents the absolute deflection for three different rail sections: 49E1, 56E1 and 60E2 (base case). The rail properties primarily influence the response at higher frequencies ($f > 800$ *Hz*) and therefore the results are shown only at the rail above the sleeper, rather than at other observation points. Below 50 *Hz*, the curves have comparable gradients, with the heaviest rail exhibiting the lowest amplitude and the lightest rail displaying the highest amplitude. The rail section size induces a similar response at all frequencies up to approximately 800 *Hz*, where all curves rapidly decay.

### 6.2. Railpad

Fig. 31 displays the response of the rail above the sleeper, computed with soft (B1), typical (base case, B2) and stiff railpads (B3). Similar to the rail behaviour, all railpad curves experience a comparable decay rate of amplitude below 50 *Hz*. Beyond this frequency, the difference between them becomes more pronounced, leading to diverging results where the maximum difference occurs between 300 – 600 *Hz*, where the

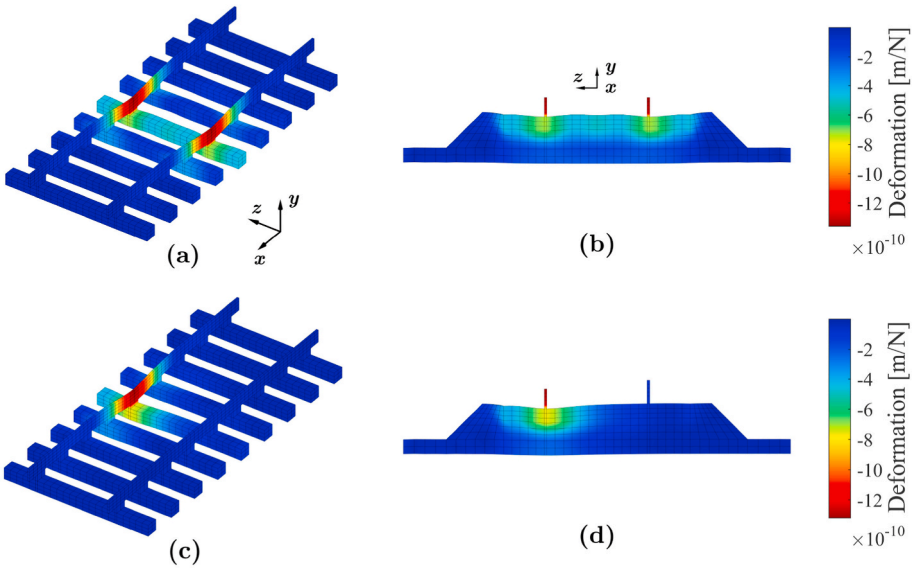


**Fig. 27.** Absolute track deformation at 320 *Hz*: (a) symmetric force model 3D view, (b) symmetric force model transversal view, (c) non-symmetric force model 3D view, and (d) non-symmetric force model transversal view. Lower components removed for visibility.

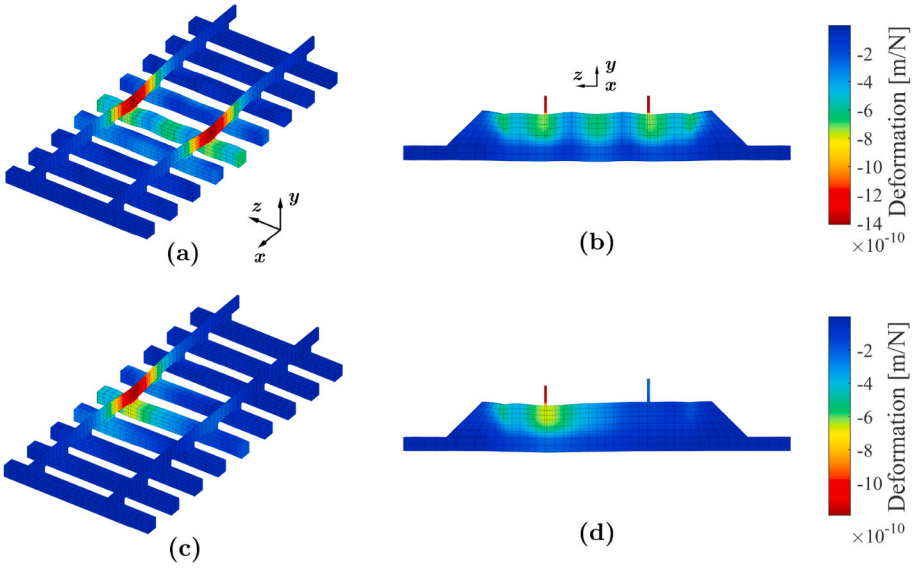


**Fig. 28.** Absolute track deformation at 440 *Hz*: (a) symmetric force model 3D view, (b) symmetric force model transversal view, (c) non-symmetric force model 3D view, and (d) non-symmetric force model transversal view. Lower components removed for visibility.

**Table 3**
Parametric simulation permutations.

| Permutation | Case of Study | |
|---|---|---|
| A3/B2/C3/D1/E2/F1/G1/H2 | – | Base parameters |
| **A123**/B2/C3/D1/E2/F1/G1/H2 | **A** | Rail: sections |
| A3/**B123**/C3/D1/E2/F1/G1/H2 | **B** | Railpad: stiffness |
| A3/B2/**C123**/D1/E2/F1/G1/H2 | **C** | Sleeper: material |
| A3/B2/C3/**D123**/E2/F1/G1/H2 | **D** | USP: stiffness |
| A3/B2/C3/D1/**E12345**/F1/G1/H2 | **E** | Ballast: stiffness and thickness |
| A3/B2/C3/D1/E2/**F1**/G1/H2 | **F** | Sub-ballast: single case |
| A3/B2/C3/D1/E2/F1/**G123**/H2 | **G** | Embankment: depth |
| A3/B2/C3/D1/E2/F1/G1/**H123** | **H** | Subgrade: stiffness |

rail mass resonates over the railpad stiffness, i.e. at the railpad frequency of resonance $f_{\text{railpad}}$. Between these frequencies, soft and stiff railpads exhibit the highest and lowest amplitude, respectively. Note that typical and stiff railpads show multiple peaks at around 300 *Hz* and 600 *Hz*, corresponding to $f_{\text{rail}}$ and $f_{\text{railpad}}$, respectively. In contrast, soft railpad response results in a low $f_{\text{railpad}}$ overlapped by $f_{\text{rail}}$, thus making the former challenging to identify. Next, at $f > 600$ *Hz*, all curves experience a rapid decay.

### 6.3. Sleeper

The sleeper effect is investigated considering three scenarios: wooden (C1), plastic (C2), and concrete (base case, C3) sleepers. To do so, results are shown at the rail above sleeper (RS) and sleeper centre (SC) observation points – see Fig. 32. All curves experience a similar and relatively constant gradient below 50 *Hz*, with identical and more flexible behaviour in C1 and C2, compared to C3. Note that the stiffness values of wooden and plastic sleepers are comparable (8.4 GPa and 8 GPa, respectively), thus explaining their similarities in the response. Above this frequency, the sleeper stiffness and density induce a change in the gradient and all curves diverge reaching their maximum difference at around 320 *Hz* ($f_{\text{rail}}$). At this frequency, the response at the rail

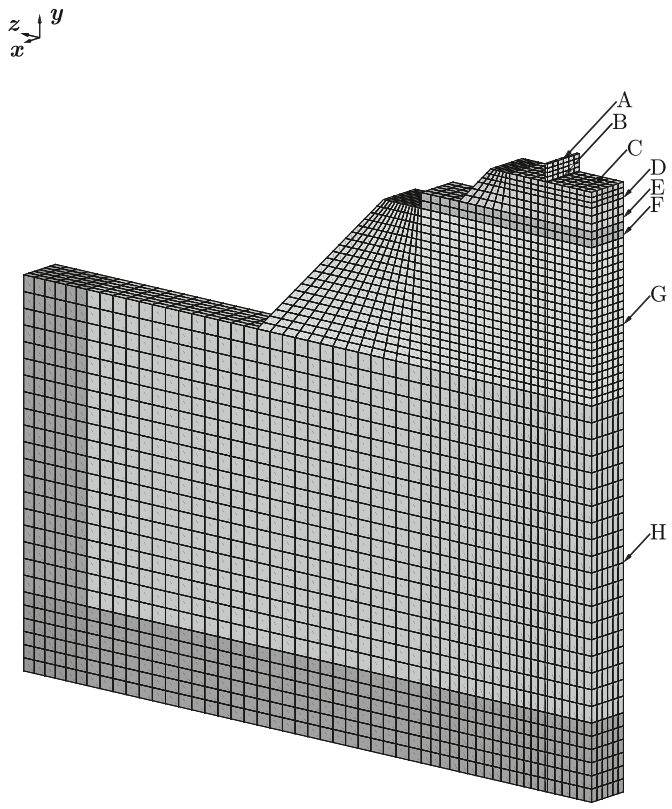


**Fig. 29.** 3D view reference cell mesh with components in permutations highlighted. Only half-track shown for visibility purposes.

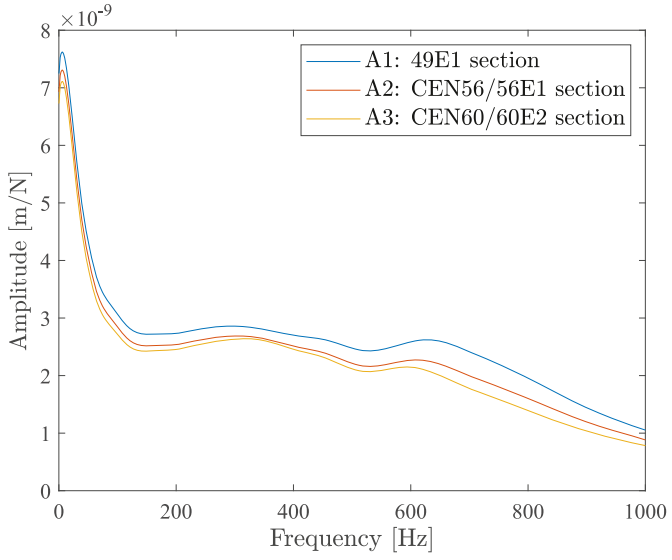


**Fig. 30.** Rail receptance above sleeper. Rail section effect.

point (RS) yields the stiffest at C3 and the softest at C1. This behaviour is opposed to the sleeper observation point (SC), where C3 and C1 yield the stiffest and softest response, respectively. Regarding C1 and C2 cases, it can be seen that the lower density of the former induces a greater deflection.

### 6.4. Under sleeper pads

The effect of Under-Sleeper Pads (USP) is explored in Fig. 33. Results are shown at the rail above sleeper and at the sleeper centre observation

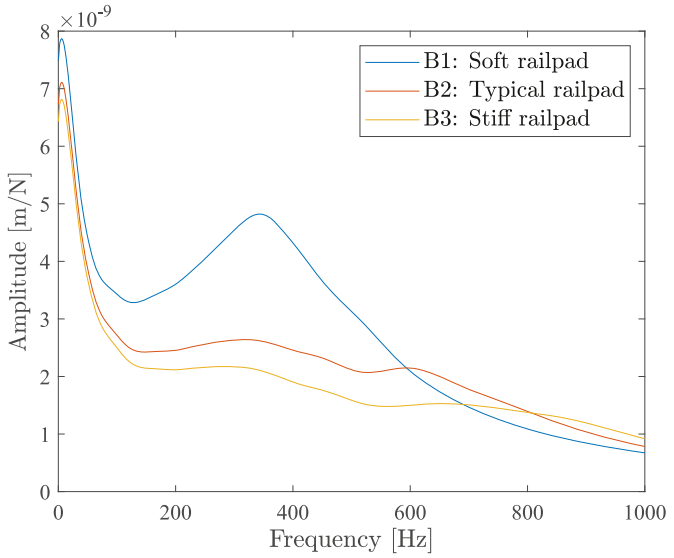


**Fig. 31.** Rail receptance above sleeper. Railpad stiffness effect.

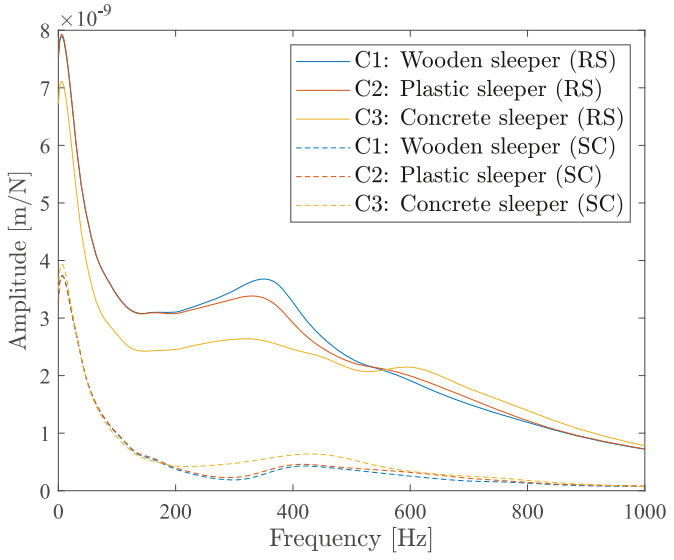


**Fig. 32.** Frequency response at rail above sleeper (RS) and sleeper centre (SC). Sleeper material effect.

points, considering three scenarios: no USP (base case, D1), soft USP (D2) and stiff USP (D3). Below 50 Hz, the gradients of all curves remain relatively stable. However, above this frequency, the gradient difference starts to increase slightly. In the $50 - 500$ *Hz* range, USP inclusion leads to a slight increase in the response amplitude. Conversely, for frequencies above 500 *Hz*, the USP scenarios generate the stiffest response, resulting in a slightly higher railpad resonance frequency ($f_{\text{railpad}}$) compared to the absent case.

### 6.5. Ballast

Fig. 34 compares the effect of the ballast stiffness at the rail above sleeper and sleeper centre observation points. Below 50 *Hz*, the ballast stiffness impact the response in a similar manner, with the soft case (E1) producing the greatest amplitude, followed by the typical (base case, E2) and the stiff ballast (E3) – all curves with comparable gradients. This behaviour persists up to approximately 300 *Hz*, the rail resonance ($f_{\text{rail}}$), where the amplitude difference among all results reaches its maximum. Above 300 *Hz*, all curves decays, first by the soft ballast, followed by the

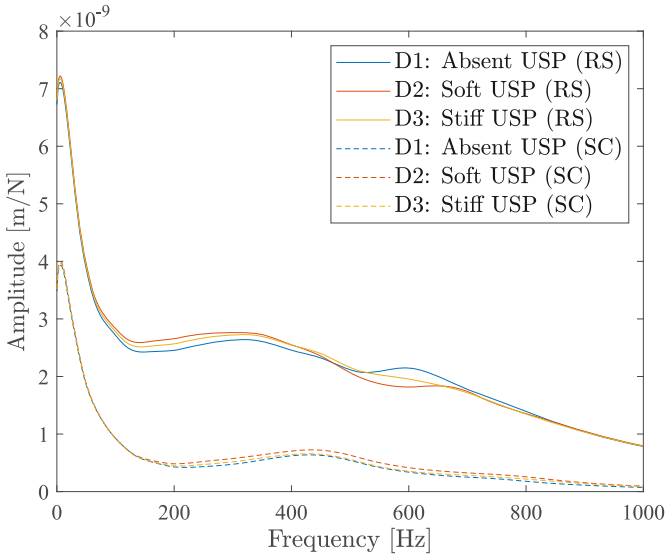


**Fig. 33.** Frequency response at rail above sleeper (RS) and sleeper centre (SC). USP effect.

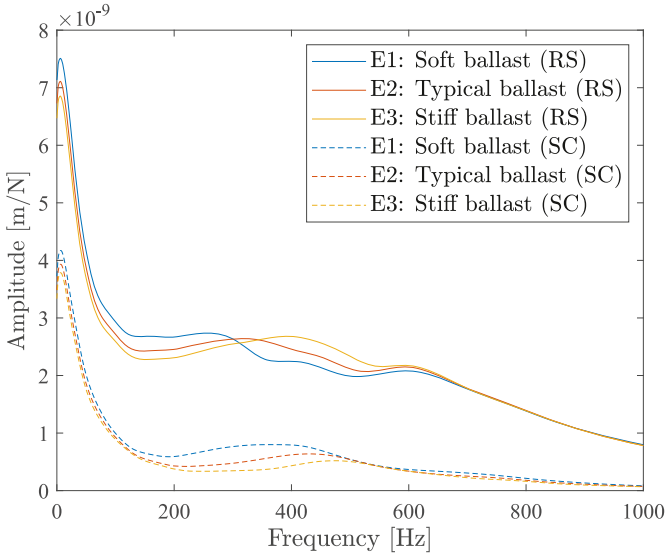


**Fig. 34.** Frequency response at rail above sleeper (RS) and sleeper centre (SC). Ballast stiffness effect.

typical and the stiff cases. Next, at around 600 *Hz* ($f_{\text{railpad}}$), all curves converge, indicating that the ballast does not affect the structure at high-frequency ranges.

In addition to the stiffness effect, ballast thickness is also investigated. Three cases are assessed: typical (E2), deep (E4) and deeper (E5) ballast. Results demonstrate the height does not significantly influence the resonant frequencies – see Fig. 35. It is observed that the ballast height leads to similar amplitudes and gradients up to approximately 50 *Hz*. However, beyond this frequency, all curves intersect at around 100 *Hz* and 200 *Hz* and ultimately converge above 400 *Hz*.

### 6.6. Embankment

Fig. 36 illustrates the effect of embankment height, considering a well compacted embankment with $E = 200$ MPa. Results are shown at the rail above sleeper point for three cases: at-grade (base case, G1), deep embankment (G2), and deeper embankment (G3). Results show the embankment implementation primarily affects the response at

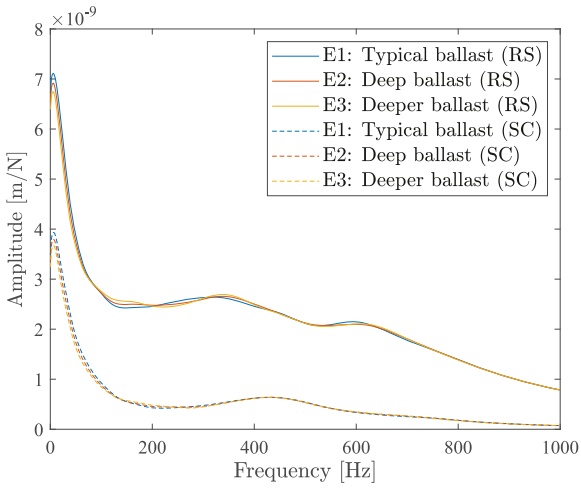


**Fig. 35.** Frequency response at rail above sleeper (RS), rail at mid-span (RM), and sleeper centre (SC). Ballast thickness effect.

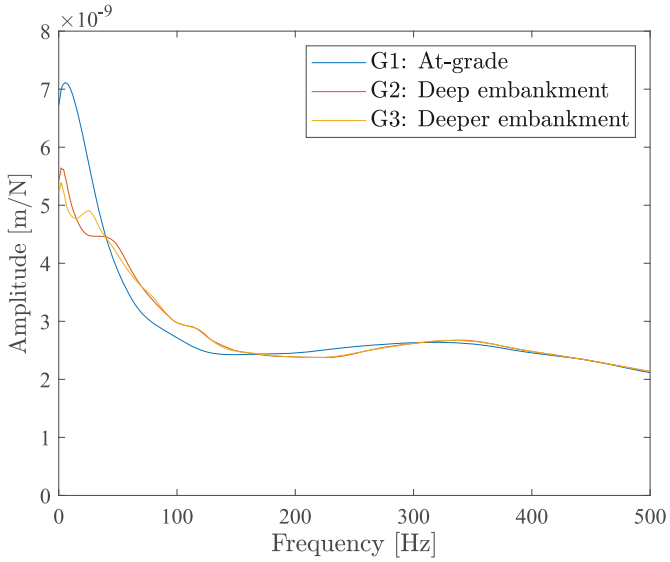


**Fig. 36.** Rail receptance above sleeper. Embankment effect.

$f < 300$ *Hz*, reducing the structure deflection and broadening the response. This occurs because the embankment is stiffer than the supporting subgrade. This behaviour is accompanied by disturbances manifested as peaks between $0 - 200$ *Hz*, representing the propagation of the response within the embankment. Also, it is observed that the embankment cases (G2 and G3) intersect the at-grade case at 50 *Hz*, 180 *Hz* and 300 *Hz*. Between the first two intersection points ($50 - 180$ *Hz*) all curves exhibit a similar gradient, with G2 and G3 displaying a higher deflection than G1. This behaviour is opposed to the second set of intersection points ($180 - 300$ *Hz*), where G2 and G3 display a stiffer response compared to G1. Overall, this behaviour likely indicates the frequency range in which the sub-ballast layer is most affected, as both the embankment and the sub-ballast has similar properties.

### 6.7. Subgrade

Finally, Fig. 37 compares the rail on support response for a soft (H1), typical (base case, H2) and stiff (H3) subgrade cases. Results show the subgrade mainly affects the response at frequencies below 300 *Hz*. Similar to the embankment effect, it can be seen that the typical and the

stiff subgrade curves intersect the soft subgrade at approximately 50 *Hz*, 180 *Hz* and 300 *Hz*. At $f < 50$ *Hz*, the stiff subgrade has the lowest deflection, followed by the typical and soft subgrade. Between $50 - 180$ *Hz*, all curves show similar behaviour, with the stiff subgrade having a slightly larger amplitude than the typical and soft cases. In contrast, at $180 - 300$ *Hz*, the soft subgrade exhibits a slightly softer deflection compared to the other subgrade cases. Overall, it is observed that both the stiff subgrade and the inclusion of embankment (see Fig. 36) greatly improves the response at lower frequency ranges. However, the latter is accompanied by additional disturbances, which do not develop when increasing the stiffness of the subgrade.

## 7. Discussion

This paper introduces new in-sights on receptance analysis and expands upon previous researches conducted in Refs. [9,12,16] by focusing on:

1. Implementing the DPM, a computationally efficient technique that allows replicating the total structural behaviour via a single slice,
2. Providing a closer approximation of both track (through complex support conditions and track's components representation) and ground dynamic behaviour via a combination of 3D FEM-PML techniques,
3. Investigating the effect of rigid foundations and symmetry conditions, and
4 Presenting an in-depth assessment of multiple track components' effect on the structure's response which allows for the definition of more detailed frequency ranges.

The related sensitivity study is used to identify the influence of specific track parameters on the entire structure. This allows for the definition of frequency ranges within which the response amplitude changes or remains constant. With this information, it is possible to identify and target particular railway issues by adjusting the track components' mechanical parameters and ultimately optimise railway system's design and maintenance operations, thus improving the total system response. Fig. 38 displays the frequency ranges where each track component has a dominant effect on the track response. For each component the horizontal bar indicates the relevant frequency range, with the colour intensity indicating the dominance of each frequency within. It can be seen that the subgrade mainly impacts frequencies around 10 *Hz* however still has some influence up to 300 *Hz*. The embankment's effect is comparable to that of the subgrade albeit with a minimal shift to higher frequency. In contrast, the ballast energy is observed between $80 - 600$ *Hz*, with its main impact at approximately 300 *Hz*. The sleeper's influence extends to the high-frequency range ($> 800$ *Hz*) however primarily affects frequencies around 350 *Hz*. Finally, the railpad and the rail affect the response above 250 *Hz* and 800 *Hz*, respectively. This behaviour is expected as they are the uppermost track components. However, the dominant effect of the railpad occurs around 600 *Hz* – a frequency close to the rail's lower limit, while the rail occurs at $> 1000$ *Hz*.

## 8. Conclusions

Railway track dynamic stiffness can be measured through receptance analysis, the relationship between track mechanical response and frequency. This parameter affects the track's dynamic response under moving train loads, elastic behaviour and noise and vibration characteristics. Thus, this paper provides two main novelties: (1) the presentation of a new numerical approach tailored to receptance calculation, and (2) a parametric study identifying the key frequencies associated with different track components.

Firstly, the numerical approach is introduced. This employs a computationally efficient 3D periodic technique coupled with perfectly matched layers solved in the frequency-wavenumber domain (3D DPM-FEM-PML). The approach allows for the simulation of complex track geometry and its dynamic wave propagation effect using an efficiently-sized domain. Next, the periodic model's ability to replicate the railway track and wave propagation dynamics is validated. Then, the 3D DPM-FEM-PML is used to study the effect of rigid foundations and symmetry conditions, both common modelling assumptions used in the modelling of track receptance. It is shown that disregarding wave propagation in the subgrade layers and below introduces significant errors, approximately $80 - 300\%$ for frequencies below 200 *Hz* and errors of around 30% for frequencies between $200 - 440$ *Hz*. Additionally, it is shown that assuming track centreline symmetry neglects some track bending modes and can lead to errors of $\approx 20\%$ up to 1000 *Hz*. Finally, the effect of the most common track components on receptance is analysed and new knowledge is presented regarding the typical frequency ranges associated with each component.

## Author statement

Angie C. Lamprea-Pineda: Methodology, Software, Validation, Investigation, Writing - Original Draft, Writing - Review & Editing.

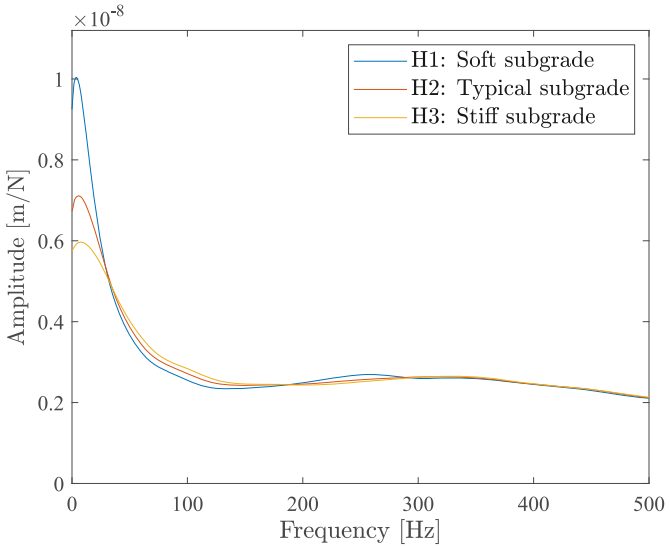


**Fig. 37.** Rail receptance above sleeper. Subgrade stiffness effect.

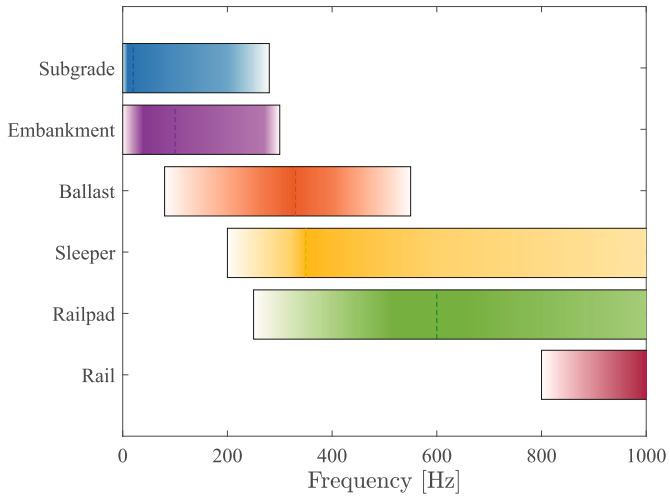


**Fig. 38.** Frequency ranges effect of each track component. Dominance within the range indicated in dashed lines.

David P. Connolly: Conceptualization, Methodology, Software, Validation, Resources, Writing - Original Draft, Writing - Review & Editing, Supervision, Funding acquisition. Alexandre Castanheira-Pinto: Conceptualization, Software, Supervision. Pedro Alves-Costa: Conceptualization, Writing - Review & Editing. Mohammed F.M. Hussein: Conceptualization, Writing - Review & Editing. Peter K. Woodward: Supervision.

## Declaration of competing interest

The authors declare that they have no known competing financial interests or personal relationships that could have appeared to influence the work reported in this paper.

## Data availability

The authors do not have permission to share data.

## Acknowledgements

The authors acknowledge the support of the University of Leeds, University of Porto, Qatar University, and the Leverhulme Trust UK (PLP-2016-270). The participation of Pedro Alves Costa was financially supported by: Base Funding - UIDB/04708/2020 and Programmatic Funding - UIDP/04708/2020 of the CONSTRUCT - Instituto de I&D em Estruturas e Construções – funded by national funds through the FCT/MCTES (PIDDAC) and Project PTDC/ECI-EGC/3352/2021, funded by national funds through FCT MCTES.

## Appendix A

Table A1 shows the material and geometrical properties of each track component considered in the simulations.

**Table A.1**
Track properties. Model refinement and sensitivity analysis

| Component | | Parameter | | Units | Case | | | | |
|---|---|---|---|---|---|---|---|---|---|
| | | | | | 1 | 2 | 3 | 4 | 5 |
| – | Track | $l_0$ | Gauge | m | 0.7175 | – | – | – | – |
| | Cell | d | Length | m | 0.6 | – | – | – | – |
| **A** | Rail | – | Layer type | – | 49E1 | CEN56/56E1 | CEN60/60E2* | – | – |
| | | $l_{yr}$ | Height | m | 0.190 | 0.210 | 0.218 | – | – |
| | | $l_{zr}$ | Width | m | 0.033 | 0.034 | 0.035 | – | – |
| | | $\eta_r$ | Loss factor | – | 0.01 | 0.01 | 0.01 | – | – |
| | | $\rho_r$ | Density | $kg/m^3$ | 7850 | 7850 | 7850 | – | – |
| | | $m_r$ | Mass | kg/m | 49 | 56 | 60 | – | – |
| | | $\nu_r$ | Poisson ratio | – | 0.3 | 0.3 | 0.3 | – | – |
| | | $E_r$ | Young's modulus | GPa | 210 | 210 | 210 | – | – |
| **B** | Railpad | – | Layer type | – | Soft | Typical* | Typical* | – | – |
| | | $l_{xrp}$ | Length | m | 0.2 | 0.2 | 0.2 | – | – |
| | | $l_{yrp}$ | Thickness | m | 0.01 | 0.01 | 0.01 | – | – |
| | | $l_{zrp}$ | Width | m | 0.035 | 0.035 | 0.035 | – | – |
| | | $\eta_{rp}$ | Loss factor | – | 0.15 | 0.15 | 0.15 | – | – |
| | | $\rho_{rp}$ | Density | $kg/m^3$ | 1000 | 1000 | 1000 | – | – |
| | | $\nu_{rp}$ | Poisson ratio | – | 0.45 | 0.45 | 0.45 | – | – |
| | | $E_{rp}$ | Young's modulus | MPa | 100 | 200 | 300 | – | – |
| **C** | Sleeper | – | Layer type | – | Wood | Plastic | Concrete* | – | – |
| | | $l_{xs}$ | Length | m | 0.2 | 0.2 | 0.2 | – | – |
| | | $l_{ys}$ | Thickness | m | 0.2 | 0.2 | 0.2 | – | – |
| | | $l_{zs}$ | Width | m | 1.3 | 1.3 | 1.3 | – | – |
| | | $d_0$ | Spacing | m | 0.6 | 0.6 | 0.6 | – | – |
| | | $\eta_s$ | Loss factor | – | 0.01 | 0.01 | 0.01 | – | – |
| | | $\rho_s$ | Density | $kg/m^3$ | 1096 | 1800 | 2500 | – | – |
| | | $\nu_s$ | Poisson ratio | – | 0.2 | 0.4 | 0.2 | – | – |
| | | $E_s$ | Young's modulus | GPa | 8.4 | 8 | 31 | – | – |
| **D** | USP | – | Layer type | – | Absent* | Soft | Stiff | – | – |
| | | $l_{xusp}$ | Length | m | – | 0.2 | 0.2 | – | – |
| | | $l_{yusp}$ | Thickness | m | 0 | 0.01 | 0.005 | – | – |
| | | $l_{zusp}$ | Width | m | – | 1.3 | 1.3 | – | – |
| | | $\eta_{usp}$ | Loss factor | – | – | 0.08 | 0.1 | – | – |
| | | $\rho_{usp}$ | Density | $kg/m^3$ | – | 800 | 800 | – | – |
| | | $\nu_{usp}$ | Poisson ratio | – | – | 0.35 | 0.45 | – | – |
| | | $E_{usp}$ | Young's modulus | MPa | – | 1.5 | 2 | – | – |
| **E** | Ballast | – | Layer type | – | Soft | Typical* | Stiff | Deep | Deeper |
| | | $w_b$ | Shoulder width | m | 0.3 | 0.3 | 0.3 | 0.3 | 0.3 |
| | | $l_{xb}$ | Length | m | 0.6 | 0.6 | 0.6 | 0.6 | 0.6 |
| | | $l_{yb}$ | Thickness | m | 0.3 | 0.3 | 0.3 | 0.4 | 0.5 |

(continued on next page)

**Table A.1** (*continued*)

| Component | | Parameter | | Units | Case | | | | |
|---|---|---|---|---|---|---|---|---|---|
| | | | | | 1 | 2 | 3 | 4 | 5 |
| | | $l_{z1b}$ | Width - Top | m | 1.6 | 1.6 | 1.6 | 1.6 | 1.6 |
| | | $l_{z2b}$ | Width - Bottom | m | 2.1 | 2.2 | 2.3 | 2.2 | 2.2 |
| | | $\eta_b$ | Loss factor | – | 0.4 | 0.4 | 0.4 | 0.4 | 0.4 |
| | | $\rho_b$ | Density | kg/m$^3$ | 1700 | 1700 | 1700 | 1700 | 1700 |
| | | $\nu_b$ | Poisson ratio | – | 0.3 | 0.3 | 0.3 | 0.3 | 0.3 |
| | | $E_b$ | Young's modulus | MPa | 150 | 220 | 290 | 220 | 220 |
| **F** | Sub-ballast | – | Layer type | – | Typical* | – | – | – | – |
| | | $w_{sb}$ | Shoulder width | m | 0.4 | – | – | – | – |
| | | $l_{xsb}$ | Length | m | 0.6 | – | – | – | – |
| | | $l_{ysb}$ | Thickness | m | 0.2 | – | – | – | – |
| | | $l_{z1sb}$ | Width - Top | m | 2.7 | – | – | – | – |
| | | $l_{z2sb}$ | Width - Bottom | m | 2.7 | – | – | – | – |
| | | $\eta_{sb}$ | Loss factor | – | 0.1 | – | – | – | – |
| | | $\rho_{sb}$ | Density | kg/m$^3$ | 1900 | – | – | – | – |
| | | $\nu_{sb}$ | Poisson ratio | – | 0.3 | – | – | – | – |
| | | $E_{sb}$ | Young's modulus | MPa | 200 | – | – | – | – |
| **G** | Embankment | – | Layer type | – | At-grade* | Deep | Deeper | – | – |
| | | $l_{xe}$ | Length | m | – | 0.6 | 0.6 | – | – |
| | | $l_{ye}$ | Height | m | 0 | 2 | 4 | – | – |
| | | $l_{z1e}$ | Width - Top | m | – | 3.3 | 3.3 | – | – |
| | | $l_{z2e}$ | Width - Bottom | m | – | 5.3 | 7.3 | – | – |
| | | $\eta_e$ | Loss factor | – | – | 0.1 | 0.1 | – | – |
| | | $\rho_e$ | Density | kg/m$^3$ | – | 2000 | 2000 | – | – |
| | | $\nu_e$ | Poisson ratio | – | – | 0.3 | 0.3 | – | – |
| | | $E_e$ | Young's modulus | MPa | – | 200 | 200 | – | – |
| **H** | Subgrade | – | Layer type | – | Soft | Typical* | Stiff | – | – |
| | | $l_{ysg}$ | Depth | m | ∞ | ∞ | ∞ | – | – |
| | | $\eta_{sg}$ | Loss factor | – | 0.1 | 0.1 | 0.1 | – | – |
| | | $\rho_{sg}$ | Density | kg/m$^3$ | 1800 | 1800 | 1800 | – | – |
| | | $\nu_{sg}$ | Poisson ratio | – | 0.35 | 0.35 | 0.35 | – | – |
| | | $E_{sg}$ | Young's modulus | MPa | 40 | 80 | 120 | – | – |

* Base parameters.

## Appendix B

In addition to vertical displacement, the track's response due to a harmonic impulse can be expressed in terms of velocity and acceleration. When measuring the response at the same point as the application of the force, point receptance, mobility, or accelerance can be determined, depending on whether displacements, velocities, or accelerations are being computed, respectively. On the contrary, when the measuring point differs from the force, the frequency responses are all transfer functions, i.e. transfer receptance, transfer mobility, or a transfer accelerance.

Fig. B.1 compares the frequency response at different rail positions, taking into account the support and symmetric loading effect. In the first case, Fig. B1(a), results are presented in terms of velocity. Alternatively, Fig. B1(b) illustrates the acceleration of the structure. Overall, the resonant frequencies identified in the displacement response (see Figs. 16 and 22) are also displayed in the velocity and acceleration results. Despite this, the minimum amplitude is found at lower frequencies in the velocity and acceleration response, and on higher frequencies in the displacement case. This is because the response is divided by the frequency and the square of the frequency in the velocity and accelerance case respectively, resulting in suppression of the amplitude at lower frequencies and amplification at higher frequencies.

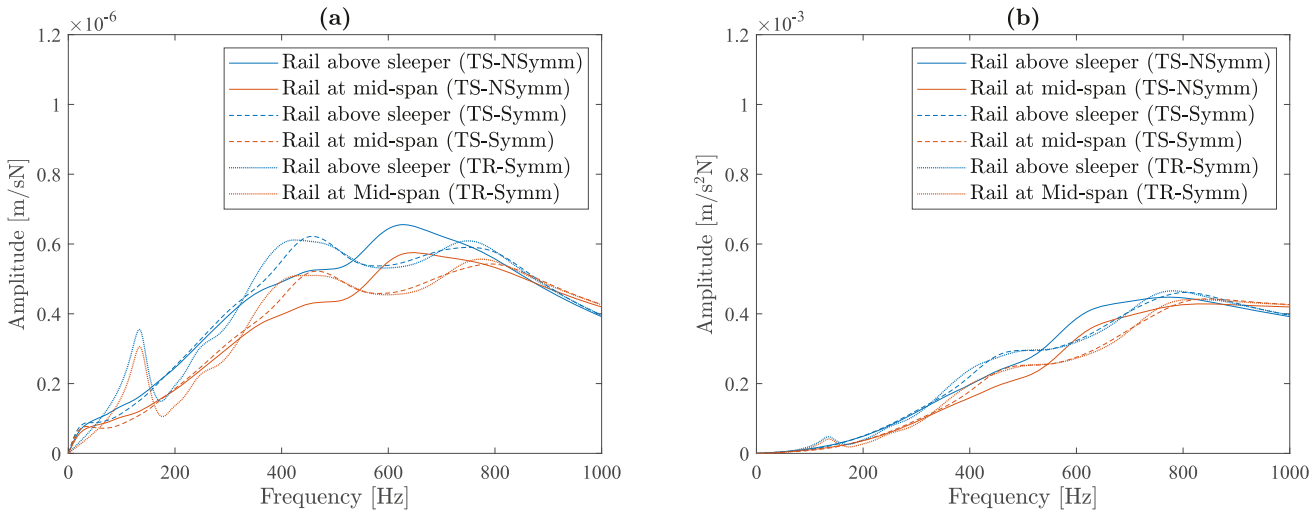


**Fig. B.1.** Track response: (a) velocities and (b) accelerations. Track on subgrade support – non-symmetric loading (TS – NSymm), track on subgrade support – symmetric loading (TS – Symm), and track on rigid support – symmetric loading (TR – Symm)

## References


[1] Berggren EG, Jahlénius Å, Bengtsson B-E, Berg M. Simulation, development and field testing of a track stiffness measurement vehicle. In: Proc. 8th int. Heavy haul conf., rio de Janeiro; 2005. p. 763–72.

[2] Berggren EG, Kaynia AM, Dehlbom B. Identification of substructure properties of railway tracks by dynamic stiffness measurements and simulations. J Sound Vib 2010;329:3999–4016. https://doi.org/10.1016/j.jsv.2010.04.015.

[3] Berggren EG. Railway track stiffness : dynamic measurements and evaluation for efficient maintenance. In: Skolan för teknikvetenskap, farkost och flyg. Kungliga Tekniska högskolan; 2009.

[4] Wang P, Wang L, Chen R, Xu J, Xu J, Gao M. Overview and outlook on railway track stiffness measurement. J Mod Transp 2016;24:89–102. https://doi.org/10.1007/s40534-016-0104-8.

[5] Morais J, Fortunato E, Ribeiro D, Calçada R, Mendes J. Railway track support condition assessment — methodology validation using numerical simulations. Eng Fail Anal 2023;152:107483. https://doi.org/10.1016/j.engfailanal.2023.107483.

[6] Zhang X, Thompson D, Jeong H, Toward M, Herron D, Jones C, et al. Measurements of the high frequency dynamic stiffness of railway ballast and subgrade. J Sound Vib 2020;468:115081. https://doi.org/10.1016/j.jsv.2019.115081.

[7] Ferreira PAAD. Modelling and prediction of the dynamic behaviour of railway infrastructures at very high speeds. Universidade Técnica de Lisboa, Instituto Superior Técnico; 2010.

[8] Grassie SL, Gregory RW, Harrison D, Johnson KL. The dynamic response of railway track to high frequency vertical excitation. J Mech Eng Sci 1982;24:77–90. https://doi.org/10.1243/JMES_JOUR_1982_024_016_02.

[9] Knothe KL, Grassie SL. Modelling of railway track and vehicle/track interaction at high frequencies. Veh Syst Dyn 1993;22:209–62. https://doi.org/10.1080/00423119308969027.

[10] Thompson D. Railway noise and vibration. Elsevier; 2009. https://doi.org/10.1016/B978-0-08-045147-3.X0023-0.

[11] Lamprea-Pineda AC, Connolly DP, Hussein MFM. Beams on elastic foundations – a review of railway applications and solutions. Transp Geotech 2022;33:100696. https://doi.org/10.1016/j.trgeo.2021.100696.

[12] Knothe KL, Wu Y. Receptance behaviour of railway track and subgrade. Arch Appl Mech (Ingenieur Arch 1998;68:457–70. https://doi.org/10.1007/s004190050179.

[13] Kouroussis G, Connolly DP, Verlinden O. Railway-induced ground vibrations – a review of vehicle effects. Int J Rail Transp 2014;2:69–110. https://doi.org/10.1080/23248378.2014.897791.

[14] Chumyen P, Connolly DP, Woodward PK, Markine V. A comparison of earthwork designs for railway transition zones. Construct Build Mater 2023;395:132295. https://doi.org/10.1016/j.conbuildmat.2023.132295.

[15] Connolly DP, Giannopoulos A, Forde MC. Numerical modelling of ground borne vibrations from high speed rail lines on embankments. Soil Dynam Earthq Eng 2013;46:13–9. https://doi.org/10.1016/j.soildyn.2012.12.003.

[16] de Man AP, Dyntrack. A survey of dynamic railway track properties and their qualities. Technische Universietit Delft; 2002.

[17] de Man AP. Pin-pin resonance as a reference in determining ballasted railway track vibration behaviour. Heron 2000;45:35–51.

[18] Oregui M, Li Z, Dollevoet R. An investigation into the modeling of railway fastening. Int J Mech Sci 2015;92:1–11. https://doi.org/10.1016/j.ijmecsci.2014.11.019.

[19] Oregui M, Núñez A, Dollevoet R, Li Z. Sensitivity analysis of railpad parameters on vertical railway track dynamics. J Eng Mech 2017;143. https://doi.org/10.1061/(ASCE)EM.1943-7889.0001207.

[20] Shen C, Deng X, Wei Z, Dollevoet R, Zoeteman A, Li Z. Comparisons between beam and continuum models for modelling wheel-rail impact at a singular rail surface defect. Int J Mech Sci 2021;198:106400. https://doi.org/10.1016/j.ijmecsci.2021.106400.

[21] Alves Costa P, Calçada R, Silva Cardoso A. Track–ground vibrations induced by railway traffic: in-situ measurements and validation of a 2.5D FEM-BEM model. Soil Dynam Earthq Eng 2012;32:111–28. https://doi.org/10.1016/j.soildyn.2011.09.002.

[22] François S, Schevenels M, Galvín P, Lombaert G, Degrande G. A 2.5D coupled FE–BE methodology for the dynamic interaction between longitudinally invariant structures and a layered halfspace. Comput Methods Appl Mech Eng 2010;199:1536–48. https://doi.org/10.1016/j.cma.2010.01.001.

[23] Charoenwong C, Connolly DP, Woodward PK, Galvín P, Alves Costa P. Analytical forecasting of long-term railway track settlement. Comput Geotech 2022;143:104601. https://doi.org/10.1016/j.compgeo.2021.104601.

[24] Charoenwong C, Connolly DP, Odolinski K, Alves Costa P, Galvín P, Smith A. The effect of rolling stock characteristics on differential railway track settlement: an engineering-economic model. Transp Geotech 2022;37:100845. https://doi.org/10.1016/j.trgeo.2022.100845.

[25] Charoenwong C, Connolly DP, Colaço A, Alves Costa P, Woodward PK, Romero A, et al. Railway slab vs ballasted track: a comparison of track geometry degradation. Construct Build Mater 2023;378:131121. https://doi.org/10.1016/j.conbuildmat.2023.131121.

[26] Alves Costa P, Calçada R, Silva Cardoso A. Ballast mats for the reduction of railway traffic vibrations. Numerical study. Soil Dynam Earthq Eng 2012;42:137–50. https://doi.org/10.1016/j.soildyn.2012.06.014.

[27] Chebli H, Clouteau D, Schmitt L. Dynamic response of high-speed ballasted railway tracks: 3D periodic model and in situ measurements. Soil Dynam Earthq Eng 2008;28:118–31. https://doi.org/10.1016/j.soildyn.2007.05.007.

[28] Germonpré M, Degrande G, Lombaert G. A track model for railway-induced ground vibration resulting from a transition zone. Proc Inst Mech Eng - Part F J Rail Rapid Transit 2018;232:1703–17. https://doi.org/10.1177/0954409717745202.

[29] Arlaud E, D'Aguiar S, Balmes E. Validation of a reduced model of railway track allowing long 3D dynamic calculation of train-track interaction. In: Comput. Methods recent adv. Geomech.. CRC Press; 2014. p. 1193–8. https://doi.org/10.1201/b17435-209.

[30] Arlaud E, Costa D'Aguiar S, Balmes E. Receptance of railway tracks at low frequency: numerical and experimental approaches. Transp Geotech 2016;9:1–16. https://doi.org/10.1016/j.trgeo.2016.06.003.

[31] Esveld C. Modern railway track. Second Edi; 2001.

[32] Dahlberg T. Track issues. In: Iwnicki S, editor. Handb. Railw. Veh. Dyn. second ed. 2006. p. 552. https://doi.org/10.1201/9781420004892.

[33] Zeng Y, Shen C, Núñez A, Dollevoet R, Zhang W, Li Z. An interpretable method for operational modal analysis in time-frequency representation and its applications to railway sleepers. Struct Control Heal Monit 2023 2023:1–26. https://doi.org/10.1155/2023/6420772.

[34] Shen C, Dollevoet R, Li Z. Fast and robust identification of railway track stiffness from simple field measurement. Mech Syst Signal Process 2021;152:107431. https://doi.org/10.1016/j.ymssp.2020.107431.

[35] Sheng X, Jones CJC, Thompson DJ. Responses of infinite periodic structures to moving or stationary harmonic loads. J Sound Vib 2005;282:125–49. https://doi.org/10.1016/j.jsv.2004.02.050.

[36] Connolly DP, Galvín P, Olivier B, Romero A, Kouroussis G. A 2.5D time-frequency domain model for railway induced soil-building vibration due to railway defects. Soil Dynam Earthq Eng 2019;120:332–44. https://doi.org/10.1016/j.soildyn.2019.01.030.
[37] Kouroussis G, Gazetas G, Anastasopoulos I, Conti C, Verlinden O. Discrete modelling of vertical track–soil coupling for vehicle–track dynamics. Soil Dynam Earthq Eng 2011;31:1711–23. https://doi.org/10.1016/j.soildyn.2011.07.007.
[38] Farooq MA, Nimbalkar S, Fatahi B. Three-dimensional finite element analyses of tyre derived aggregates in ballasted and ballastless tracks. Comput Geotech 2021;136:104220. https://doi.org/10.1016/j.compgeo.2021.104220.
[39] Shan Y, Zhou S, Wang B, Ho CL. Differential settlement prediction of ballasted tracks in bridge–embankment transition zones. J Geotech Geoenviron Eng 2020;146:04020075. https://doi.org/10.1061/(ASCE)GT.1943-5606.0002307.
[40] Connolly DP, Dong K, Alves Costa P, Soares P, Woodward PK. High speed railway ground dynamics: a multi-model analysis. Int J Rail Transp 2020;8:324–46. https://doi.org/10.1080/23248378.2020.1712267.
[41] Castanheira-Pinto A, Colaço A, Ruiz JF, Alves Costa P, Godinho L. Simplified approach for ground reinforcement design to enhance critical speed. Soil Dynam Earthq Eng 2022;153:107078. https://doi.org/10.1016/j.soildyn.2021.107078.
[42] Sadri M, Lu T, Steenbergen M. Railway track degradation: the contribution of a spatially variant support stiffness - global variation. J Sound Vib 2020;464:114992. https://doi.org/10.1016/j.jsv.2019.114992.
[43] Sadri M, Lu T, Steenbergen M. Railway track degradation: the contribution of a spatially variant support stiffness - local variation. J Sound Vib 2019;455:203–20. https://doi.org/10.1016/j.jsv.2019.05.006.
[44] Gupta S, Degrande G, Chebli H, Clouteau D, Hussein MFM, Hunt HEM. A coupled periodic FE-BE model for ground-borne vibrations from underground railways. Lisbon, Portugal: III Eur. Conf. Comput. Mech.; 2006. https://doi.org/10.1007/1-4020-5370-3_212. 212–212.
[45] Chebli H, Othman R, Clouteau D, Arnst M, Degrande G. 3D periodic BE–FE model for various transportation structures interacting with soil. Comput Geotech 2008;35:22–32. https://doi.org/10.1016/j.compgeo.2007.03.008.
[46] Hussein MFM, Hunt HEM. Modelling of floating-slab track with discontinuous slab: Part 1: response to oscillating moving loads. J Low Freq Noise Vib Act Control 2006;25:23–39. https://doi.org/10.1260/026309206777637339.
[47] Hussein MFM, Hunt HEM. Modelling of floating-slab track with discontinuous slab: Part 2: response to moving trains. J Low Freq Noise Vib Act Control 2006;25:111–8. https://doi.org/10.1260/026309206778494283.
[48] Hussein MFM. A comparison between the performance of floating-slab track with continuous and discontinuous slabs in reducing vibration from underground railway tunnels. In: 16th int. Congr. Sound vib. Pol. Krakow; 2009.
[49] Forrest JA. Modelling of ground vibration from underground railways. University of Cambridge; 1999.
[50] Floquet G. Sur les équations différentielles linéaires à coefficients périodiques. Ann Sci l'École Norm Supérieure 1883;12:47–88. https://doi.org/10.24033/asens.220.
[51] Chebli H, Othman R, Clouteau D. Response of periodic structures due to moving loads. Compt Rendus Mec 2006;334:347–52. https://doi.org/10.1016/j.crme.2006.04.001.
[52] Clouteau D, Arnst M, Al-Hussaini TM, Degrande G. Freefield vibrations due to dynamic loading on a tunnel embedded in a stratified medium. J Sound Vib 2005;283:173–99. https://doi.org/10.1016/j.jsv.2004.04.010.
[53] Auersch L. Simple and fast prediction of train-induced track forces, ground and building vibrations. Railw Eng Sci 2020;28:232–50. https://doi.org/10.1007/s40534-020-00218-7.
[54] Auersch L. Train-induced ground vibration due to the irregularities of the soil. Soil Dynam Earthq Eng 2021;140:106438. https://doi.org/10.1016/j.soildyn.2020.106438.
[55] Johnson SG. Notes on perfectly matched layers (PMLs). abs/2108.0. ArXiv; 2021. p. 1–16. 10969193.
[56] Basu U. Explicit finite element perfectly matched layer for transient three-dimensional elastic waves. Int J Numer Methods Eng 2009;77:151–76. https://doi.org/10.1002/nme.2397.
[57] Basu U, Chopra AK. Perfectly matched layers for time-harmonic elastodynamics of unbounded domains: theory and finite-element implementation. Comput Methods Appl Mech Eng 2003;192:1337–75. https://doi.org/10.1016/S0045-7825(02)00642-4.
[58] Lopes Patrícia, Alves Costa Pedro, Calçada Rui, Cardoso António Silva. Numerical modeling of vibrations induced in tunnels: a 2.5D FEM-PML approach. In: Xia H, Calçada Rui, editors. Traffic induced Environmental Vibrations and Controls: Theory and Application; 2013. p. 133–66.
[59] François S, Schevenels M, Lombaert G, Degrande G. A 2.5D displacement-based PML for elastodynamic wave propagation. Comput Mech 2010:2. –3.
[60] Lopes P, Alves Costa P, Ferraz M, Calçada R, Cardoso AS. Numerical modeling of vibrations induced by railway traffic in tunnels: from the source to the nearby buildings. Soil Dynam Earthq Eng 2014;61–62:269–85. https://doi.org/10.1016/j.soildyn.2014.02.013.